DOCTORAL THESIS

UNCOVERING THE ROLE OF FREE VOLUME IN BIOMATERIALS AND BIOLOGICAL MATTER

ENEKO AXPE

SUPERVISOR: FERNANDO PLAZAOLA
CO-SUPERVISOR: JOSE ANGEL GARCÍA

2015

eman ta zabal zazu

Universidad del País Vasco
Euskal Herriko Unibertsitatea

ACKNOWLEDGEMENTS

Eskerrik asko ama, umetxo bat nintzenetik etxerako lanekin laguntzeagatik. Nire buru zoro, sortzaile eta hiperaktiboa bideratzea ez zen lan erreza izango. Eskerrik asko aita, badakit ilusio berezia egiten dizula tesi honek. Eskerrik asko Nagoretxu eta amama Elo zuen maitasunagatik.

Gogoratzen dut 5 urte inguru nituenean, eskolako Azucena irakasleak nire amari batzar batean esan ziola nagusitan *delincuente* bat izango nintzela. Eskerrik asko Azucena, *visionaria* bat izan zinen.

Eskerrik asko Beurko Institutuko Javi Ibarra Fisika irakasleari, Fisikaren legeekin gozatzen irakasteagatik.

Fisikako lizentziaturaren infernu horretan Javi Ibarraren bidea jarraitu nuen Juan Mari Agirregabiriari esker; eskerrik asko Juan Mari. Eta eskerrik asko, Aitor Bergara, eman zenizkidan aholkuak oso baliogarriak izan zirelako infernua zerua bilakatzeko.

Esku artean duzun tesi honen bidaia magikoa izan da niretzat. Izugarri ikasi dut, eta ez bakarrik Fisika, Biologia, Biofisika, Ehun-ingenieritza, Polimeroak edota Bionanoteknologiari buruz. Ikerkuntzan, edo beste edozein lan esparrutan, inguruan dituzun pertsonak garrantzitsuena dela ikasi dut. Pertsonak zaintzen badituzu, lan taldearen giroa zaintzen baduzu, denborarekin, emaitzak helduko dira. Batzutan, ondokoaren irribarre bat *paper* bat publikatzea baino beharrezkoagoa da.

Eta asko izan dira bidaia honetan alboan izan ditudan pertsonak, eskerrik asko infinituak bidaian ezagutu ditudan lagun horiei. Lehenik eta behin, niretzat garrantzitsuena izan den pertsona horrentzat: eskerrik asko bihotz erraldoi hori izateagatik, Maite. Eskerrik asko Anabel, Inari, Mireia, Lulu, Luca, David, Iraultza, Garaio, Popi, Janire, Libe, Edu, Jorge, Mattin, Rosa, Dani, Raul, Olalla eta departamentuko beste guztiei… lankide ezinhobeak zarete, ekipo!

Eskerrik asko Ane, porque en cierta medida tú también has sido parte de esta tesis.

Nire kolaboratzaile guzti-guztiei ere bai: eskerrik asko. Aritz, Nuria, Joni, Tamara, Ruben, etabar. Eta nola ez, kasualitatez Biologiaren unibertsoan sartu ninduen lagun zahar horri… eskerrik asko benetan, Ainara.

Agur bero bat Buli, Luis Leon, Vilas eta Felix Goñiri, gazte ausarti horren ideiak entzuteagatik eta zuen bulegoko ateak zabalik uzteagatik.

I am also very grateful to Mina Roussenova (University of Bristol, UK) for the help with the positron source and the writing of the thesis. I am thankful for the help with the lipid sample preparation to Petri Sane (Aalto University, Finland) and Ilpo Vattulainen (Tampere University of Technology, Finland). Thank you Jerzy Kansy (Silesian University of Technology, Poland) for your useful help with your program LT_Polymers.

I would like to thank all the people I met during my research stays at the University of Oxford in 2014 and in 2015, thanks a lot for your kind attention. Specially, you guys were very nice to me: Marein, Valeria (¡eres un sol!), Sonia Trigueros, Amir, Ibon, Antonio… thanks a lot! Muchas gracias Sonia Contera por darme esta magnífica oportunidad de hacer las estancias en Oxford, de recibirme con los brazos abiertos y de ayudarme tanto en todo.

Fernando, eskerrik asko aukera hau emateagatik, bene-benetan. Normalean berba txarren bat entzuten da tesi zuzendariei buruz hitz egiterakoan eta nire kasuan kontrakoa da. Nahiz eta oso lanpetuta egon Errektoreorde lanetan, beti izan zara oso adeitsua nirekin eta behar izan zaitudanean, hortxe egon zara, nahiz eta email edo telefonoaren bestaldean izan. Baita zuri ere Jose Angel, zer esanik ez… zelako pazientzia izan duzun nirekin! Beti zaude gure alboan, lan egiteko eta laguntzeko prest. Eskerrik asko! Nire ideia guztiak entzun dituzue bien artean, eta nire bide propioa zelan garatu ere irakatsi didazue... Milesker!

Azkenik eta bihotzez eskerrak eman nahi dizkiot hezkuntza sistema publikoa posible egiten duzuen pertsona guztiei. Familia xume batean jaio nintzen eta hezkuntza sistema publikoa eta Unibertsitate publikoari esker goi mailako prestakuntza bat jaso dut. Nire helburua orain munduko Unibertsitate onenetan nire prestakuntza jarraitzea da, eta noizbait sistema publikoak emandako guztia berari, eta bereziki Euskal Herriko Unibertsitateari, bueltatzea da.

This thesis has been carried out thanks to a predoctoral fellowship funded by the Basque Government.

“Bizi bihar hilko bazina bezala,
ikasi betiko biziko bazina bezala.”
Mahatma Gandhi

INDEX

Chapter 1: **POSITRON ANNIHILATION LIFETIME SPECTROSCOPY: POSITRON, POSITRONIUM AND FREE VOLUME ……………………………... 13**

1.1 The positron source …………………………………………………………... 13

1.2 The bio-sample holder for PALS measurements ………………………….. 17

1.3 The PAL spectrometer ………………………………………………..……... 19

1.4 The positron life (and lifetime) in soft matter ………………………..……... 21

1.5 Positron lifetime analysis and calculation of free volume size …………... 25

Chapter 2: **THE CONCEPT OF FREE VOLUME ……………………………….. 29**

2.1 The concept of free volume in the Ancient Greece ……………………..…. 29

2.2 The first scientific evidence of the free volume ……………………………. 30

2.3 The development of the concept ………………………………...………… 31

2.4 The current definition of free volume in soft matter ……………………… 34

2.5 The importance of the free volume holes ………………………………….. 38

Chapter 3: **LINK BETWEEN FREE VOLUME HOLE SIZE AND SHAPE MEMORY PROPERTIES IN SHAPE MEMORY POLYMERS FOR BIOMEDICAL APPLICATIONS ……………………………………………….. 39**

3.1 Materials and sample preparation …………………………………………… 42

  3.1.1 Materials ………………………………………………………………… 42

  3.1.2 Sample Preparation …………………………………………………… 43

3.2 Cytotoxicity assay …………………………………………………………….. 44

3.3 Shape memory properties …………………………………………………… 47

3.4 Free volume hole sizes ……………………………………………………….. 55

3.5 Relation between free volume and shape memory properties …………… 57

3.6 Conclusions ………………………………………………………………….. 60

Chapter 4: **THE ROLE OF THE FREE VOLUME HOLE SIZE IN TISSUE ENGINEERING MATERIALS ……………………………………………………. 63**

4.1 Materials and sample preparation …………………………………………… 67

  4.1.1 Chitosan and chitosan/CNTs solutions preparation ………….. 67

  4.1.2 Sample preparation for AFM imaging …………………………….. 68

    - 4.1.3 Scaffold fabrication 69
- 4.2 Scanning Electron Microscopy (SEM) 70
- 4.3 Positron Annihilation Lifetime Spectroscopy (PALS) 71
- 4.4 Atomic Force Microscopy (AFM) 75
    - 4.4.1 AFM imaging 76
    - 4.4.2 Force spectroscopy 77
- 4.5 Conclusions 81

Chapter 5: **THE EFFECT OF CERAMIDE IN THE FREE VOLUME OF DPPC LIPID MEMBRANES 83**
- 5.1 Materials and sample preparation 85
    - 5.1.1 Materials 85
    - 5.1.2 Membrane preparation 85
- 5.2 Differential Scanning Calorimetry (DSC) 86
- 5.3 Positron annihilation lifetime spectroscopy (PALS) 88
- 5.4 Molecular dynamics simulations 93
- 5.5 Comparison of MD simulations and PALS results 98
- 5.6 Conclusions 101

Chapter 6: **FIRST PALS STUDY FOR THE CHARACTERIZATION OF LIVING CELLS 103**
- 6.1 3D Cell cultures 107
- 6.2 Immunofluorescence microscopy 109
- 6.3 Free volume hole size measurements 111
- 6.4 Conclusions 116

Chapter 7: **FINAL CONCLUSIONS 117**

LIST OF PUBLICATIONS 119

REFERENCES 121

CHAPTER 1

POSITRON ANNIHILATION LIFETIME SPECTROSCOPY: POSITRON, POSITRONIUM AND FREE VOLUME

Positron annihilation lifetime spectroscopy (PALS) is an experimental technique widely used in Materials Science for characterizing mainly open volume defects at the atomic level by measuring the lifetime of positrons within the sample [1.1]. In the last few decades, its use in soft materials characterization is especially remarkable as it is the only technique capable to measure quantitatively the dynamic intermolecular free volume at the molecular level in soft condensed matter [1.2]. In particular, the more recently application of PALS in biological matter and soft biomaterials is the basis of the present thesis. In the introduction the fundamental principles of PALS and the bio-PAL spectrometer of the Nuclear Techniques Laboratory of the UPV/EHU employed in all the PALS experiments of the thesis are described.

1.1 The positron source

^{22}Na radioisotope has been used as positron source in all the PALS experiments of the present thesis. This is the most conventional positron source in PALS experiments for many reasons:

(i) As a PALS experiment takes hours or days and the ^{22}Na radioisotope half-life is 2.605 years, the flux of positrons is almost constant during the experiment.

(ii) When ^{22}Na radioisotope decays, there exists an almost simultaneous emission of a positron and a γ photon of 1.274 MeV. This means that if we are able to detect this released photon, we are setting the t=0 of the positron lifetime.

(iii) Stable ^{22}Ne is released in the ^{22}Na radioisotope decay (see the decay scheme of ^{22}Na in Figure 1). No radioactive isotope is released in ^{22}Na radioisotope decay.

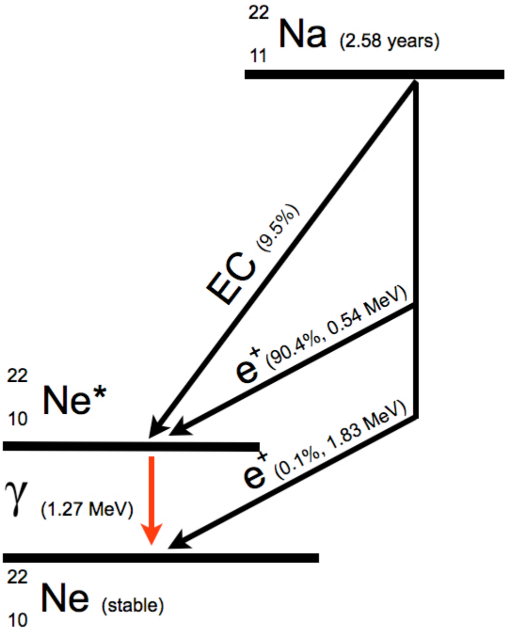

Figure 1 Decay scheme of ^{22}Na radioisotope adapted from [1.3].

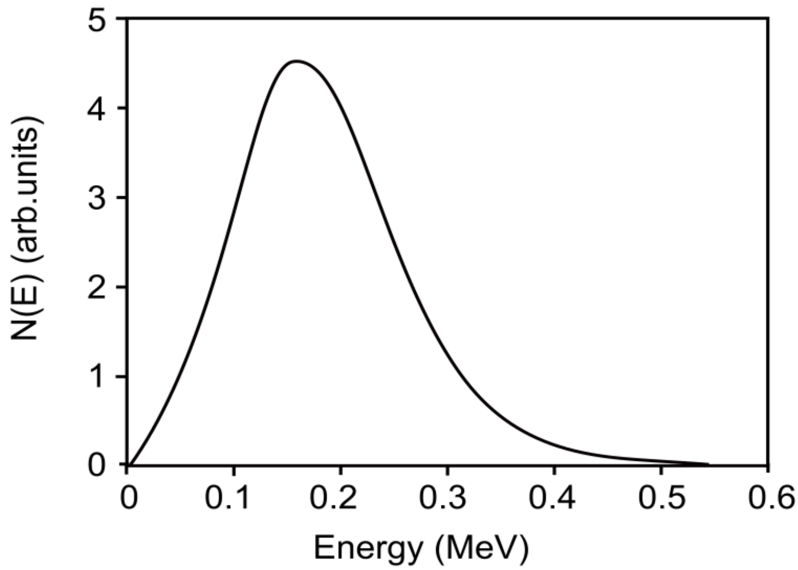

Figure 2 Energy spectrum of positrons emitted by ^{22}Na adapted from Reference [1.4].

^{22}Na decays as follows:

$$^{22}\mathrm{Na} \rightarrow {}^{22}\mathrm{Ne} + e^{+} + \nu_{e} + \gamma$$

As shown in Figure 1, the ^{22}Na decays to ^{22}Ne (excited state) in the 99.9% of the events by positron emission (90.4%) or electron capture (EC, 9.5%), and, in the 0.1% of the events, to ^{22}Na (ground state). So, in the 99.9% of the events, the ^{22}Ne in the excited state decays to the ground state emitting a 1.274 MeV. As explained before, this will be the t=0 of the lifetime of the positron (the gamma ray is emitted only 3 ps after the birth of the positron). The energy spectrum of positrons emitted by ^{22}Na is plotted in Figure 2. As we can see, it is continuous ranging from 0 to one end-point energy of around 0.54 MeV.

We fabricated two different sealed sources (in the following called *robust* or *R1* and *thin* or *T1*) for measuring liquids/biological samples following a recipe provided by Mina Roussenova, PhD (Bristol University, UK) in a private communication after the meeting in the Positron and Positronium Chemistry 10 in Slovakia. We used a 7.5-μm kapton foil CS Hyde (USA) and another 75 μm kapton DuPont (USA) foil for the *robust* source and two 7.5-μm kapton foils CS Hyde (USA) for the *thin* source. For the experiments, the positron source is sandwiched by two identical samples. The ^{22}NaCl (PerkinElmer, USA) solution was deposited drop by drop just in the middle of one of the kapton foils. After drying it by using an infrared lamp, the two kapton foils were stick with a double-sided sticky kapton tape from CAPLINQ (Canada) containing a 0.3 cm diameter hole in the middle for keeping the ^{22}Na in touch with the foils. We left the sources to seal properly by pressing them with heavy metallic weights for a couple of days. We checked that the sources were completely sealed wiping them all over with a wet tissue (wet wipe test). After we thoroughly checked that there was no contamination on the tissue, we proceed to locate it in a small amount of water (we used small amounts of water in order to minimize the amount of contaminated water if the source does leak). Source passed both, the wet wipe and the water tests. The activity of the obtained positron sources was 15 μCi.

1.2 The bio-sample holder for PALS measurements

Positrons emitted by the ^{22}Na source penetrate into the sample. The penetration is expressed as follows [1.5]:

$$P(x) = \mu_{imp} e^{-\mu_{imp} x}$$

where x is the depth of the sample, and μ_{imp} the absorption coefficient. The following relationship has been obtained empirically [1.6]:

$$\mu_{imp} = 16 \frac{\rho}{E_{max}^{1.4}}$$

where E_{max} is the maximum energy of the emitted positrons [MeV], and ρ is the density of the target sample [g/cm^3].

For the design of the bio-sample holder and by using this equation, we calculated the positron penetration depth in water, obtaining 0.27 mm. Taking into account this result, we designed (Figure 3) and fabricated a bio-sample holder made of pure aluminium (99.9%) from Goodfellow, UK:

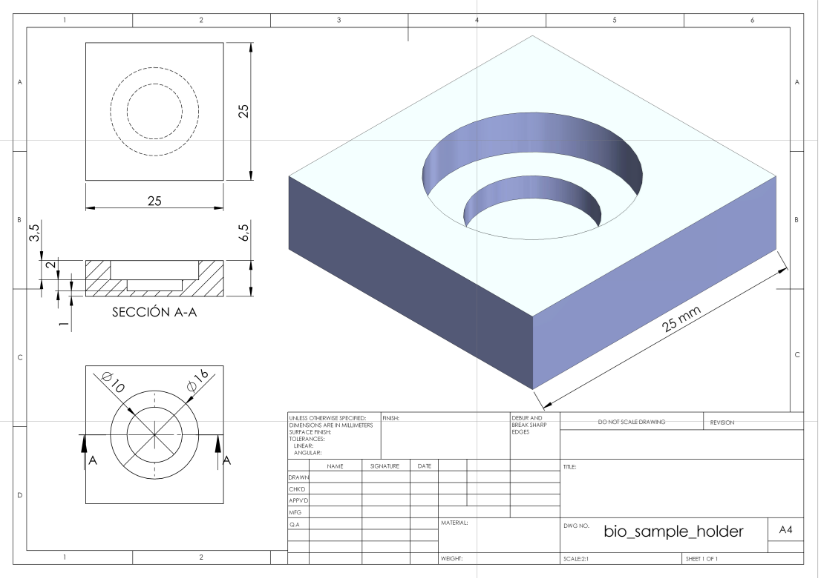

Figure 3 Design of the bio-sample holder.

The bio-sample holder was designed with the depth (for 2 identical samples) of ~2mm, to ensure that all the positrons annihilate inside the sample. We also designed the holder bearing in mind the surface size of the sealed source (10 mm · 11 mm). The sealed source fits perfectly between the two identical samples inside of the holder.

Next, we made small holes for implementing a heater and a temperature sensor for temperature experiments. The temperature of the sample is controlled by an Eurotherm (United Kingdom) 3508 programmable temperature control system equipped with a variable power supply provided by SALICRU (Bilbao, Spain), a 100W FIREROD® cartridge heater from Watlow Europe (Kronau, Germany), and a PT-100 CS5 (1|5) temperature sensor purchased from TC S.A. (Madrid, Spain). This PT-100 and the heater were installed inside the bio-sample holder. The positron source is sandwiched between two identical samples.

Valentin Toyos (technician, Department of Electricity and Electronics, UPV/EHU) was a key person in the design and fabrication of the bio-sample holders. Around 40 identical holders have been used in this work.

1.3 The PAL spectrometer

As shown in Figure 4 and explained in section 1.1, the detection of a 1.274 MeV γ photon is the “start” signal of the lifetime of the positron, and the 511 keV γ photon, result of the annihilation between the positron and an electron of the sample, is the “stop” signal. BC-422 Saint Gobain (Hiram, OH, USA) plastic scintillators detectors (SC) are coupled with H1949-50 photomultiplier tubes (PMT) made by Hamamatsu Photonics (Tokyo, Japan), to convert these high-energy photons into electrical signals. The scintillators and photomultipliers used in this thesis are placed in a vertical performance inside a FFD-1402 refrigerator from Radiber S.A. (Barcelona, Spain) as shown in Figure 4. The spectrometer used a conventional ORTEC (Oak Ridge, TN, USA) fast-fast coincidence mode, with a 567 Ortec TAC/SCA, 583B Ortec CF DIFF DISC, 556 Ortec High Voltage PS, DB463 Ortec delay and MCA3-p7882 Com. Tec. (Germany), with a resolution (full width half maximum) of around 260 ps. In the fast-fast coincidence mode the electric signals obtained by the photomultipliers travel from the PMT to the constant-fraction discriminator (CFDD). These electronic modules discriminate the energy of the "selected" photons for the start and stop signals, and give the time signal. The output of each CFDD is passed through a delay and feeds one input (start or stop) of the time to amplitude converter (TAC). The TAC gives pulses with amplitudes proportional to the time difference between the start and stop pulses. The delay modules are used to increase the time difference between both pulses (increasing the voltage of the TAC pulses). Finally, the multichannel analyzer (MCA) module is used to collect the pulses and to give the positron lifetime spectrum. The MCA is connected to a PC, where the *Maestro* software is installed to collect and to save the spectra. The number of counts on each measured spectrum of this thesis was on the order of millions (more than 2.5 millions in all the cases).

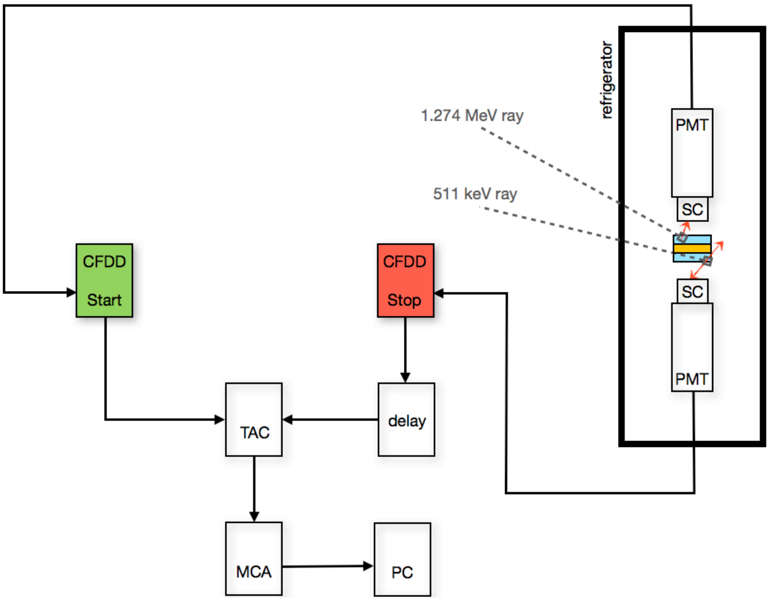

Figure 4 PALS scheme based on a conventional fast-fast coincidence system and picture of the bio-PALS system (the part corresponding to the sample holder, scintillators and photomultipliers) installed inside the refrigerator.

1.4 The positron life (and lifetime) in soft matter

The positron was theoretically predicted by Dirac in 1928 [1.7] and observed experimentally by Anderson in 1933 [1.8], demonstrating for the first time the existence of the antimatter. The positron is the antiparticle of the electron. The positron has the same mass (9.11×10^{-31} kg), the same spin (1/2) and equal but opposite charge ($q = + 1.602 \times 10^{-19}$ C) of the electron.

In PALS experiments, the positron source is typically sandwiched by two identical samples. When the positron is emitted during the decay of the ^{22}Na source gets into the sample and loses energy by inelastic collisions with the atoms/molecules of the sample material. This process (called thermalization) takes place in 1-10 ps in condensed matter and can reach 100 ps in soft matter [1.2]. In this lastcase, in the *trajectory regime* during the thermalization, a “spur” of free electrons, free radicals and positively charged ions is created by ionizations due to the liberated kinetic energy of the positron when it collides with the atoms/molecules of the sample material. Next, when the positron has not enough energy to make more ionizations, it stops in the *terminal spur* and become thermalized [1.9]. After thermalization occurs, in the terminal spur, the positron is surrounded by free electrons, free radicals and positive ions and can:

(i) annihilate as a free positron with an electron in the spur (the lifetime of the positron in this case varies from 0.1 ns to 0.5 ns, depending on the material).

(ii) recombine wih an electron of the spur to form Positronium (Ps). [1]

The Ps is then formed in the *terminal spur* by a thermalized positron and a thermalized electron. It is important to note that the Ps formation is in competition with the recombination of the electron and a positive ion in the spur, the “removing” of the electron by solvent molecules (electron scavengers), and the diffusion of the electron out of the spur.

---

[1] Note that in this thesis the formation of the Ps is assumed to happen by the Spur model (Ps is formed only formed once the positron is thermalized) [1.9]. The Ore model [1.10] assumes that the Ps is formed when a positron that has not been thermalized yet, picks up an electron from a molecule to form Ps. The Ore model is useful for explaining Ps formation in simple gases, but it is not valid for Ps formation in liquids and solids.

We call Ps to a meta-stable state between a positron and an electron. Its radius is 1.59 Å long [1.2] and it has been described as “the lightest atom in the Universe”, as it is relatively similar to the hydrogen atom, but having a positron instead a proton. The existence of Ps was firstly probed in 1951 by Deutsch [1.11]. There exist two different states of Ps: the para-Positronium (p-Ps) or singlet state (S=0), in which the spins of the positron and the electron are anti-parallel, and the ortho-Positronium (o-Ps) or triplet state (S=1), where the spins of the positron and the electron are parallel. From spin statistics it is known that the formation ratio of o-Ps to p-Ps is equal to 3:1. In vacuum, the p-Ps has a mean lifetime of 125 ps and decays in 2 photons, while the o-Ps decays in 3 photons and has a mean lifetime of 142 ns [1.2]. Within soft matter, o-Ps mainly annihilates by *pick-off* annihilation, decreasing the o-Ps lifetime to 1-5 ns and decaying in 2 photons as shown in Figure 5.

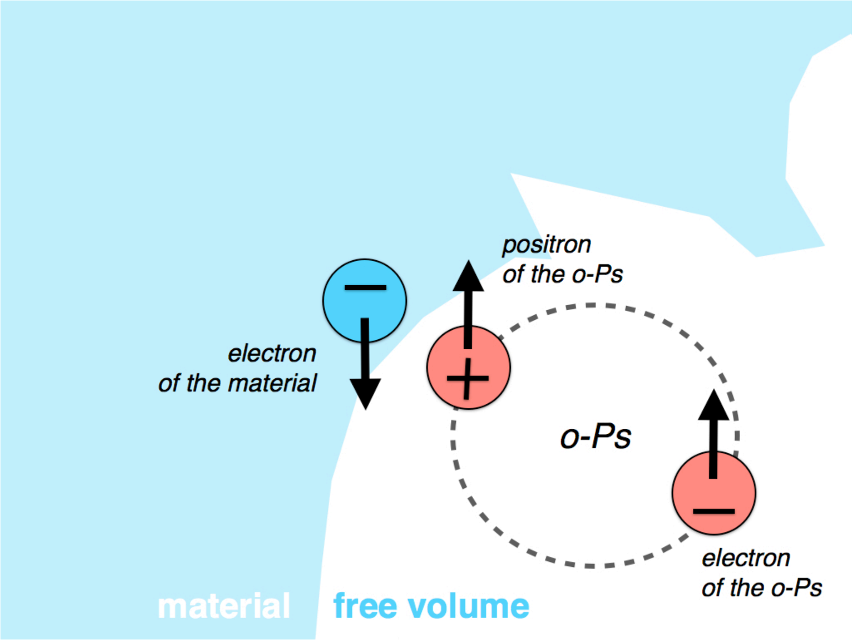

Figure 5 Pick-off annihilation scheme. The positron of the o-Ps inside of the free volume hole annihilates with an electron of the material´s wall. The spin of the electron of the material is antiparallel to the spin of the positron of the o-Ps.

In molecular solids, once the o-Ps is formed, it is localized in low electron density regions as sub-nanometric local free volume holes [1.12]. These free volume holes arise due to an irregular packing, density fluctuations or topological constrains. When the o-Ps is localized within one of this holes, it “tries” to expand the hole due to the repulsion forces between the electron of the o-Ps and the electrons of the molecules surrounding the free volume hole. In rigid molecular solids, the o-Ps are trapped in pre-existing local free volume holes and does not change the shape and size of the hole. If an o-Ps is trapped in a free volume hole, it is localized there, in that single hole, and it “hits” continuously the electron-“wall” of the hole until *pick-off* occurs.

The *pick-off* annihilation occurs between the positron of the o-Ps and an electron (with an anti-parallel spin in respect to the positron) of the “wall” of the hole. The molecules of the medium surrounding the free volume hole are considered the “wall” of the hole. When the local material density is low enough as in some liquids, once the o-Ps is formed, it is self-trapped, and a sub-nanometric free volume cavity (also called void, or *bubble*) is formed around the o-Ps due to the Coulomb and exchange repulsions between the electron of the o-Ps and the electrons of the molecules of the liquid. The radius of these cavities is around few angstroms.

1.5 Positron lifetime analysis and calculation of free volume size

Once we collect the data in the PC (see Figure 4 and section 1.3), we analyze the spectra for obtaining the free volume hole sizes within the sample. In Figure 6. a typical spectrum collected for a soft matter sample is shown, where Y axis corresponds to the number of measured counts in logarithmic scale. The software used for the analysis is the widely used open software LT_Polymers [1.13]. The typical fit of the spectrum performed with the LT program is done using three exponentials, which is typical for polymers. The exponential with the steepest slope in log scale corresponds to the shorter lifetime. It is related to the p-Ps lifetime (τ_1). The second steepest one, has a lifetime of about 400 ps and corresponds to positrons annihilating in the sample (τ_2). Finally, the exponential with smallest slope corresponds to o-Ps annihilation via pick-off (τ_3). The longest lifetime is the one we have used to determine the size of the free volume holes. Note that in some studies more than an o-Ps lifetime is reported, but this is not our case. For all the samples analyzed in this thesis, no extra τ_4 was detected, as far as the fit variance was not optimal when fixed a forth lifetime. The source component is always extracted (382 ps, corresponding to the positron lifetime in kapton). In the experiments of this thesis, the R1 source contributed with 31.6% to the spectrum, and in the case of the T1 source contributed with 19.8%.

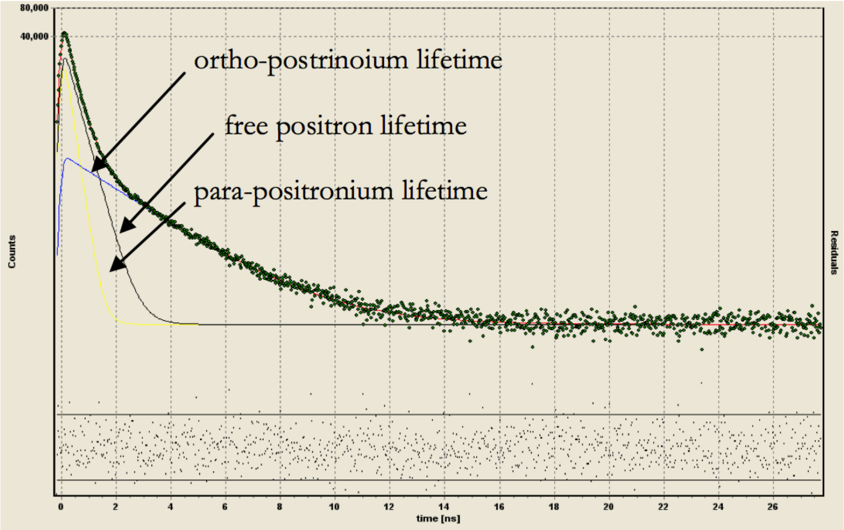

Figure 6 Typical LT spectrum corresponding to a soft matter sample. The fit is usually made by three exponentials (free positrone lifetime, p-Ps lifetime and o-Ps lifetime). Note that in some soft matter samples exist more than a single exponential corresponding to the o-Ps lifetime.

The assistance during the visit of Prof. Jerzy Kansy (the creator of the LT_Polymers software) in 2011 to our laboratory was very helpful. The LT program is an exceptional, user-friendly software that provides the mean o-Ps and distribution value of lognormal functions in comparison with other excellent programs as PositronFit. The obtained o-Ps lifetime is inversely proportional to the overlap of the o-Ps density $\left|\psi_{o-Ps}(r)\right|^2$ and the surrounding electron density n(r) [1.14]:

$$\frac{1}{\tau_{o-Ps}} = \lambda_{o-Ps} = \pi r_0^2 c \int \left|\psi_{o-Ps}(r)\right|^2 \rho(r) d^3 r$$

where τ_{o-Ps} is the positron lifetime, λ_{o-Ps} is the positron annihilation rate, r_0 is the electron radius and $\rho(r)$ is the electron density. The positron lifetime is obtained as an electronic density test. Larger the free volume hole, longer positron lifetime. The exact solutions of the wave functions and electron densities are a quite complex quantum mechanical problem. However, a relatively simple equation is widely used for calculating the free volume hole radius from the o-Ps lifetime: the Tao-Eldrup equation [1.15,1.16]. It considers a simple model in which the o-Ps particle lies in a spherical well with an infinite potential barrier radius. This model assumes a homogeneous electron layer with a thickness of $\Delta R = R_0 - R$ inside the wall, where R_0 is the radius of the infinite spherical potential and R is the free volume hole radius. Corrections of the Tao-Eldrup model have been published for large [1.17] or cylindrical shaped free volumes [1.18], among others. The analytical relationship between the o-

Ps lifetime and the radius of the free volume hole within a spherical approximation is:

$$\tau_{o-Ps}(ns) = \frac{1}{2}\left[1 - \frac{R}{R_0} + \frac{1}{2\pi}\sin\left(\frac{2\pi R}{R_0}\right)\right]^{-1}$$

where ΔR is an empirical parameter that was determined by fitting measured lifetimes with known hole sizes in molecular materials. Until now, the best fitted value is 1.66 Å [1.19].

Once introduced the positron and the positronium and the PALS technique (for further information about PALS applications in soft matter see references [1.20-1.22]), in the next chapter the free volume is deeply described in order to understand its nature and its importance in some biomaterials and Biology.

CHAPTER 2

THE CONCEPT OF FREE VOLUME

Free volume properties play a key role in several physical and mechanical characteristics of many materials (including some biomaterials). Nevertheless, it is quite difficult to find a standard definition for the free volume in the literature, probably due to its imprecise conceptual nature. In this chapter, the free volume is explained and defined based on the thorough bibliographic review of the development of the concept.

2.1 The concept of free volume in the Ancient Greece

The free volume concept is long-standing. In the Ancient Greece, the atomists held that there exist two fundamentally different kinds of realities composing the natural world: atoms and empty space [2.1].

"Nothing exists except atoms and empty space, everything else is opinion."

Democritus (*ca*. 460 – 370 BC)

Atomists believed that atoms (from the Greek adjective *ἄτομον*, 'indivisible') move about in an infinite void. They considered empty space as necessary condition for local motion: *"without unoccupied places, where could bodies move into?"* [2.1].

Furthermore, it has been suggested that the concept of void by Democritus is that of the (temporarily) unfilled regions between atoms rather than a conception of an infinite void [2.1,2.2]. Naturally, these ideas were founded in Philosophy rather than in scientific evidence.

2.2 The first scientific evidence of the free volume

To the best of the knowledge of the author of the present thesis, the oldest scientific report that deals with the concept of free volume was published in 1913 when Batschinki introduced the following empirical equation for the fluidity (the inverse of viscosity μ) of liquids [2.3]:

$$\frac{1}{\mu} = A\left(v - v_{s0}\right)$$

where A is a constant depending on the fluid, v is the volume of a liquid and v_{s0} is a "*limit of volume*" for the liquid. v_{s0} was extrapolated from a linear diagram with zero fluidity and it obtained a value at the fusion point between the solid and the liquid values. The difference $v-v_{s0}$ has been considered as the free volume in the liquid, even though the author did not use this term.

2.3 The development of the concept

In 1931, Eyring defended the idea of existing molecular-sized free volume holes between molecules in liquids: "*Since to form a hole the size of a molecule in a liquid requires almost the same increase in free energy as to vaporize a molecule, the concentration of vapor above the liquid is a measure of such ``molecular'' holes in the liquid.*" [2.4]. In fact, the free volume theory of the liquid state was developed by Eyring himself and Hirschfelder [2.5] in 1937, when they proposed the existence of *"holes"* in their model of binary liquids. One year later, this idea was followed by Lennard-Jones and Devonshire [2.6] in their cell method for pure liquids.

After the stop probably caused by the World War II, the 50´s were fruitful again in the development of the free volume theory. In 1950, Irving and Kirkwood showed that the free volume theory can be derived from the general principles of statistical mechanics [2.7]. Kirkwood and Salsburg branded the free volume theory as an "*intuitively plausible model (…) that has provided a useful approximate description of the thermodynamic properties of pure liquids*". They extended the free volume theory of the liquid to multicomponent fluid mixtures in 1952 [2.8]. One year before, two formulas that have become important over time in Polymer Physics were published. Although the authors did not make any specific mention to the free volume in the article that presents the Flory-Fox equation [2.9], the reader can make out the existence of some kind of free volume. On the other hand, in the Doolittle equation [2.10] the free volume is straight referred:

$$\eta = Ae^{B/(v_f/v_0)}$$

here, η was the coefficient of viscosity, A and B were two characteristics of the liquid and v_f/v_0 was called by Doolittle the "*relative free-space*". The free volume (or "free-space") was defined by Doolittle as follows: "*The "free-space" in a liquid is considered by us to be that space seemingly arising from the total thermal expansion of the liquid without change of phase. Relative free-space is therefore the fractional increase in volume resulting from expansion and is defined as:*

$$\frac{v_f}{v_0} = \frac{(v - v_0)}{v_0}$$

where v_f= volumen of free-space per gram of liquid at any temperature; v_0= volumen of 1 gram of liquid extrapolated to absolute zero without change of phase; and v= volumen of 1 gram of liquid at any temperature". Based on Doolittle´s equation, the article "*Molecular transport in liquids and glasses*" published in 1959 by Cohen and Turnbull [2.11] related the self-diffusion constant D in a liquid with the free volume V_f:

$$D = Ae^{\gamma V^*/V_f}$$

being A and γ constants, and v^* the minimum volume required of the void for diffusive displacement of a particle. In this case, the main idea was that the diffusion of a particle may happen only if next to the particle exists a free volume greater than a minimum size v^*. Free volumes smaller than this critical size do not contribute to diffusion. About this critical size, the authors pointed out: “*It is shown that data on self-diffusion in some simple van der Waals liquids and liquid metals are described satisfactorily by our relation with v^* near the molecular volume for the van der Waals liquids and near the volume of the ion, corresponding to the highest valence state, for the metals.”*. The authors related a local free volume with each molecule and assumed a distribution of local free volumes. The equation indicates that the self-diffusion constant is proportional to an exponential of the ratio between the size of the diffusion molecule and the free volume per molecule in the liquid.

In short, they proposed a revolutionary idea: free volume regulates molecular transport. It was the birth of the so-called “free volume theory” and it has been a point of departure for free volume theories developed later. Interestingly, although the theory was designed to explain the behavior of liquids (viewed as a whole of uniform hard spheres), it has had more impact in the field of polymers.

Since the 50’s, the number of publications about free volume in scientific journals had grown exponentially as shown in Figure 1.

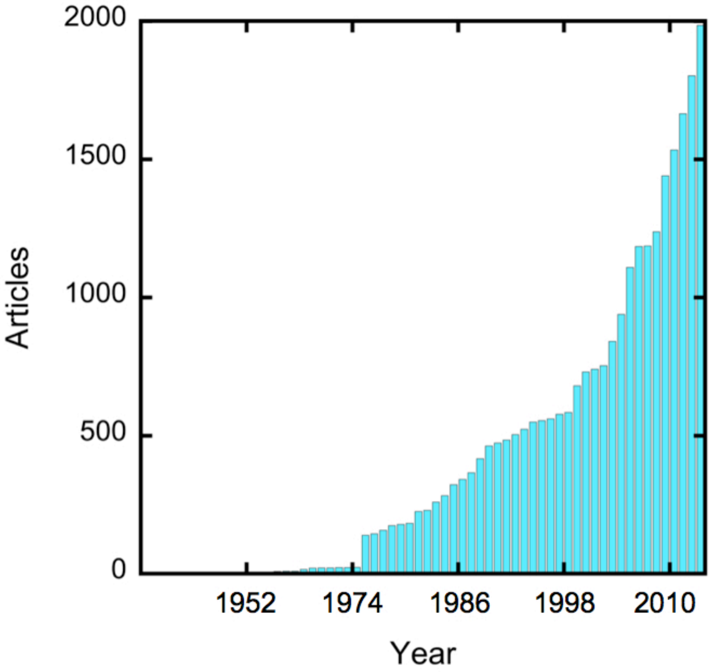

Figure 1 Number of articles about free volume published per year since 1950 in PubMed (Medline).

2.4 The current definition of free volume in soft matter

To the best of the author´s knowledge there is not any standard definition for the free volume in the literature, probably due to its imprecise conceptual nature. The free volume is usually defined in statistical mechanical models, so its definition is theory dependent. The author of this thesis strongly recommends the doctoral thesis of Mina Roussenova (University of Bristol) [2.12] for further reading about the free volume in soft matter, which has been also very helpful for the writing of this section.

Atoms and molecules do not fill completely the total specific volume (V) of a certain solid or liquid. There exists an unoccupied volume between the molecules named free volume (V_f) [2.13]:

$$V_f = V - V_{occ}$$

V_{occ} is the occupied volume by atoms and/or molecules. It is not simple to define this occupied volume. As is well known, a molecule is a system of moving particles (nuclei and electrons) that stay unified by electrostatic and magnetic forces. There is thus no any fixed form for each molecule, neither a form at all. However, representing a molecule as a solid figure is strongly justified because its usefulness in solving several chemical, physical, mechanical and biological problems. In this sense, although the simplest way to define the *occupied volume* would be the van der Waals volume, the most common definition of the *occupied volume* is given as [2.14]:

$$V_{occ} = V_W + V_{int}$$

being V_W the molecular volume (van der Waals volume) and V_{int} the interstitial free volume.

Note that the van der Waals volume is the volume of a hard sphere used to model a single atom. In the case of a molecule, it is the volume enclosed by the van der Waals surface. This is composed of the spheres for individual atoms with their intersecting sections removed. With this, the van der Waals volume of a molecule is smaller than the sum of the van der Waals volumes of the atoms forming the molecule. The Group Contribution Method developed by Bondi [2.15] defines the distance between the centers of these spheres (atoms) forming the molecule as the bond length. In short, the van der Waals volume is the volume occupied by molecules impenetrable to other molecules with normal thermal energies [2.14,2.16,2.17].

In an amorphous body, even in a "perfect" packing at T = 0K, there will appear an interstitial free volume. Surprisingly to the author, this interstitial free volume is considered as part of the occupied volume in the literature. For polymeric crystals, Bondi found a semi-empirical relation [2.18]:

$$V_{occ} = V_c(0K) \approx 1.3V_W$$

1.3 is a factor assumed to be an universal constant arising due to the packing densities of polymeric crystals. $V_c(0K)$ is the volume of a polymeric crystal at T = 0K. Of course, this relation is too simple. First, not all polymers are packing equally. Second, the relation is not taking into account the molecular vibrations (that increase with the temperature). In spite of this, it is a widely spread model.

In the literature the free volume is named in fact the excess free volume, which arises due to the static and dynamic structural disorder in amorphous systems. In fact, computational simulations of amorphous polymers highlight that the empty volume is constituted by a large number of multi-interconnected sub-nanometric size free volume holes [2.19]. In the Figure 2 [2.20] are represented some free volume holes (molecular voids), for a better understanding of this concept.

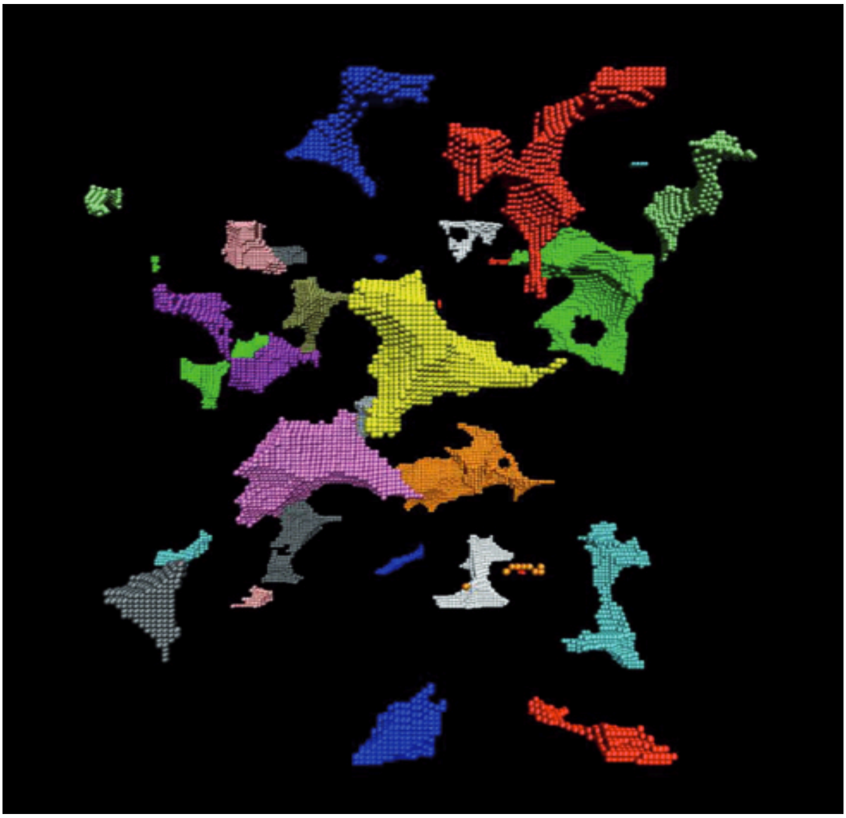

Figure 2 Snapshot of molecular voids in anhydrous maltopentose (310 K) showing the irregular void shapes. The voids have been differently colored to easily distinguish between them [2.20].

In the present thesis, we define the free volume holes as the irregularly shaped, subnanometric, holes that together form the total excess free volume (V_f) inside an amorphous body. We have measured the size (within a spherical approximation) and distribution (the larger the distribution, the larger the difference between the sizes of these holes) of these free volume holes by applying PALS, inserting ortho-Positroniums in the holes as probe molecules.

2.5 The importance of the free volume holes

It has been demonstrated that free volume holes play an important role in several properties of soft materials: viscoelastic flow [2.21], packing and ordering [2.22], self-diffusion [2.23], guest molecule diffusion [2.24] or glass transition [2.25], among others.

The following chapters contain novel PALS studies that uncover several free volume properties of polymers for biomedical applications, biopolymers for tissue engineering applications, biological membranes and living cells.

CHAPTER 3

LINK BETWEEN FREE VOLUME HOLE SIZE AND SHAPE MEMORY PROPERTIES IN SHAPE MEMORY POLYMERS FOR BIOMEDICAL APPLICATIONS.

Shape-memory polymers (SMP) are smart polymers that have the ability to return from a stable temporary (deformed) shape to a permanent (original) shape by cause of an external stimuli as temperature change [3.1], light irradiation [3.2], electrical stimulation [3.3], immersion in water [3.4], pH change [3.5], exposure to alternating magnetic fields [3.6], etc. SMPs have current and potential applications in aerospace technology [3.7], smart clothing [3.8], packaging [3.9], energy [3.10], household products [3.11] and medicine [3.12]. The acquisition of shape-memory properties is a combination of a stable polymer network and an adjusted and reversible switching transition of the polymer. The thermally-induced shape memory effect is the most extended for industrial and biomedical applications. The shape memory effect in thermoresponsive SMPs takes place above a characteristic temperature, named transition temperature (T_{trans}). When this temperature is reached, the polymer is able to recover the original shape.

Polymers are classified as crystalline, amorphous or semicrystalline, depending on the degree of crystallinity. Semicrystalline polymers have both crystalline and amorphous regions. The crystallization conditions permit to control the semicrystalline structure, and therefore the properties of the network of the SMPs that determine the original shape. Depending on the degree of crystallinity of the polymer, this switching temperature (the shape memory transition temperature) could be the glass transition temperature (T_g) or the melting temperature (T_m). If it is possible, it is more desirable to have a semicrystalline SMP to employ T_m as T_{trans}, because it is easier to predict and control than T_g, as well as T_m induces a more defined transition than T_g.

Polycyclooctene (PCO) is a thermally induced shape memory polymer, where the T_{trans} corresponds with the T_m. PCO is a semicrystalline polymer that exhibits excellent shape memory properties when the macromolecular chains are properly crosslinked. The required chemically crosslinked structures can be obtained using (i) a monofunctional peroxide (cytotoxic, risky for medical applications) [3.13] or (ii) by ionizing radiation as gamma rays [3.14,3.15] (non-cytotoxic, tested in the present study). Both processes originate free radicals capable to take off a hydrogen atom from the polymer. In this way, polymeric macroradicals react and recombine obtaining a crosslinked network [3.16]. Nonetheless, a growth in crosslink density usually generates a reduction in the crystallization temperature of the polymer, thus crystallites become shorter and can be dispersed in the crosslinked matrix [3.17]. So, the balance between the elasticity due to the crosslinked structure, and the thermal induced molecular switching of polymer chains with temperature above and below T_m, determines the shape memory response [3.18].

With all this, it is logical to hypothesize that there exists a relation between crosslinks and mobility of the polymer chains that induces the shape recovery. As the mobility of the polymer chains depends on the free volume holes within the polymer, the free volume hole size within the polymer might play an important role in the crosslinked structure, crystallinity and thus, shape memory effect of the gamma irradiated PCO shape memory polymer samples.

In recent years, PALS has been successfully applied to determine the free volume size in thousands of polymers, in fact (and as explained in previous chapters), it is a unique technique to measure the size and distribution of the subnanoscopic, local, and dynamic free volume holes. In this way, PALS has been demonstrated that the free volume plays a key role in mechanical, thermal, relaxation and diffusion properties of polymers. In this chapter, to analyze the relation between free volume hole size and shape memory, PALS and thermomechanical analysis (TMA) were utilized to test the relation between the changes in the size of the free volume holes as function of temperature and shape memory properties of the samples. Already in 1996 Ito et al. [3.19] studied the free volume properties of different shape memory polymers measured by

PALS. But in the present study free volume hole size values were further compared with the gel fraction and shape recovery ratio of different PCO-irradiated samples (irradiated at 25, 50, 75, and 200 kGy).

This chapter shows a preliminary approach to link free volume holes and shape memory properties in shape memory polymers with potential biomedical applications. Specifically, (i) it is studied the structure, free volume and shape memory properties relationship, in order to physically explain the shape recovery at the nanoscale for the design and rationally control the macroscopic shape memory properties of these materials and (ii) it is proved the noncytotoxicity of the gamma-irradiated PCO, opening the window on biomedical applications of this material.

3.1 Materials and sample preparation

3.1.1 Materials

VestenamerVR 8012 (Evonik) in pellet form, which is a 99.5% purity low broad molecular weight polyoctenamer (PCO) consisting on linear and cyclic macromolecules with 80% of its double bonds arranged in a crystallizable trans configuration, was used as received, without any previous purification step. In order to show the cytotoxicity of PCO crosslinked with peroxides we used as crosslinking agent dicumyl peroxide (DCP) from Aldrich, which is 98.0% purity solid crystalline monofunctional peroxide.

3.1.2 Sample Preparation

All the samples were prepared by Nuria García-Huete (BCMaterials) in the Laboratory of Macromolecular Chemistry in the UPV/EHU by the following protocol; to obtain the sample crosslinked with peroxide, polycyclooctene (PCO) Vestenamer® 8012 and 1 wt % dicumyl peroxide (DCP) were blended using a Haake Rheomix 600 mixing chamber at 70 °C previous to the preparation of the polymer sheet under identical conditions to those of PCO, as explained below.

PCO sheets were manufactured by compression molding under pressure of 100 bars (using a hydraulic press with thermostatically controlled plates) in a 1.5-mm thickness flat mold, at 160°C for 20 min. Two Teflon sheets were placed on both sides of the mold to reduce the surface roughness of the so-obtained PCO sheets. The obtained 50 mm X 50 mm X 1.5 mm sheets were cooled to room temperature in the mold under constant pressure.

Rectangular-shaped samples (length = 50 mm, width= 40 mm, and thickness = 1.5 mm) were cut from molded sheets of PCO, packaged and sealed under vacuum. These PCO sheets were irradiated by gamma rays in a ^{60}Co radiation facility (NÁYADE Irradiation Plant of CIEMAT, Madrid, Spain). A nonirradiated sample was used as reference for comparison with the irradiated samples. In a previous work [3.15] gel content was determined after gamma irradiation by Soxhlet extraction in cyclohexane. Furthermore, thermal properties were evaluated before and after Soxhlet extraction by means of Thermogravimetric Analysis

(TGA) and Differential Scanning Calorimetry (DSC). In Table 1 are listed the gel fraction determined by Soxhlet extraction and the thermal properties measured before Soxhlet extraction.

Sample	Rad. Dose (kGy)	Gel Fract. (wt%)	T_m (ºC)	ΔH_m (J/g)	Cry. (%)	T_d (ºC)
PCO-0	0	0	57.5	69.7	30.3	461.8
PCO-25	25	21.3	57.6	69.7	30.3	463.7
PCO-50	50	47.6	58.3	64.3	28.0	462.4
PCO-75	75	83.7	56.3	62.6	27.2	463.1
PCO-200	200	94.6	52.5	52.6	22.8	458.1

Table 1 Radiation dose, gel fraction and thermal properties of the samples [3.15].

3.2 Cytotoxicity assay

The indirect cytotoxicity evaluation was carried out according to the ISO 10993-5 standard test method in the Department of Physics of the University of Minho (Portugal) by Clarisse Ribeiro and Prof. Lanceros-Méndez, by following this protocol:

The samples were immersed in a 24-well tissue culture polystyrene plate with DMEM [containing 1 g L^{-1} glucose (Gibco) supplemented with 10% FBS (Biochrom) and 1% P/ S (Biochrom)], at 37 °C in a 95% humidified air containing 5% CO_2 and incubated for 24 h. A 20% of dimethylsulfoxide (DMSO; Sigma Aldrich) was used as a positive control and the cell culture medium was employed as negative control.

At the same time, the MC3T3-E1 preosteoblast cells were seeded in the 96-well tissue culture polystyrene plate at the density of 3×10^4 cells mL^{-1} and incubated for 24 h to allow cell attachment on the plate. After 24 h, the culture medium from the 96-well tissue culture polystyrene plate was removed and the as prepared extraction media were added to the wells (100 μL). Afterward, the cells were incubated for 24 h and 72 h and after each time, the evaluation of the cell viability was quantified with 3-(4,5-dimethylthiazol-2-yl)-2,5-diphenyltetrazolium bromide (MTT) assay.

The MTT assay measures the mitochondrial activity of the cells, which reflects the viable cell number. At each time point, the medium of every well was removed and fresh medium containing 10% MTT solution (stock solution of 5 mg MTT mL^{-1} in PBS; Sigma Aldrich) was added. The viable cells with active metabolism convert MTT into a purple colored formazan product. After 2 h of incubation, the MTT crystals were dissolved with DMSO and the optical density was measured at 570 nm. All quantitative results were obtained from four replicate samples and controls and were analyzed as the average of viability ± standard deviation (SD). The percentage of cell viability was calculated from the following equation:

$$\text{Cell viability (\%)} = \frac{\text{Absorbance of sample}}{\text{Absorbance of negative control}} \times 100$$

This assay evaluated and compared the cytotoxicity of four different PCO samples: PCO (not irradiated), PCO+1%DCP (sample crosslinked with peroxide), and the gamma irradiated samples PCO-25 (dose: 25 kGy) and PCO-200 (dose: 200 kGy). The effects of polymer extract medium on the metabolic activity of MC3T3-E1 preosteoblast cells were evaluated using the MTT assay after 24 h and 72 h (Figure 1).

According to the ISO standard 10993-5, when the cell viability reduction is larger than the 30%, the samples are considered cytotoxic. Therefore, the sample PCO+1%DCP is cytotoxic, while non-irradiated PCO and gamma irradiated samples are non-cytotoxic. So, thermo-active gamma irradiated PCO emerges as a non-cytotoxic alternative contrasting to cytotoxic shape memory PCO crosslinked via dicumyl peroxide (as shown in Figure 1) due to its metabolic activation into alkoxy radicals [3.20]. The absence of residual peroxide and related decomposition products opens biomedicine related potential applications of this shape memory polymer, such as their use as cell culture or smart scaffolds for tissue engineering [3.21].

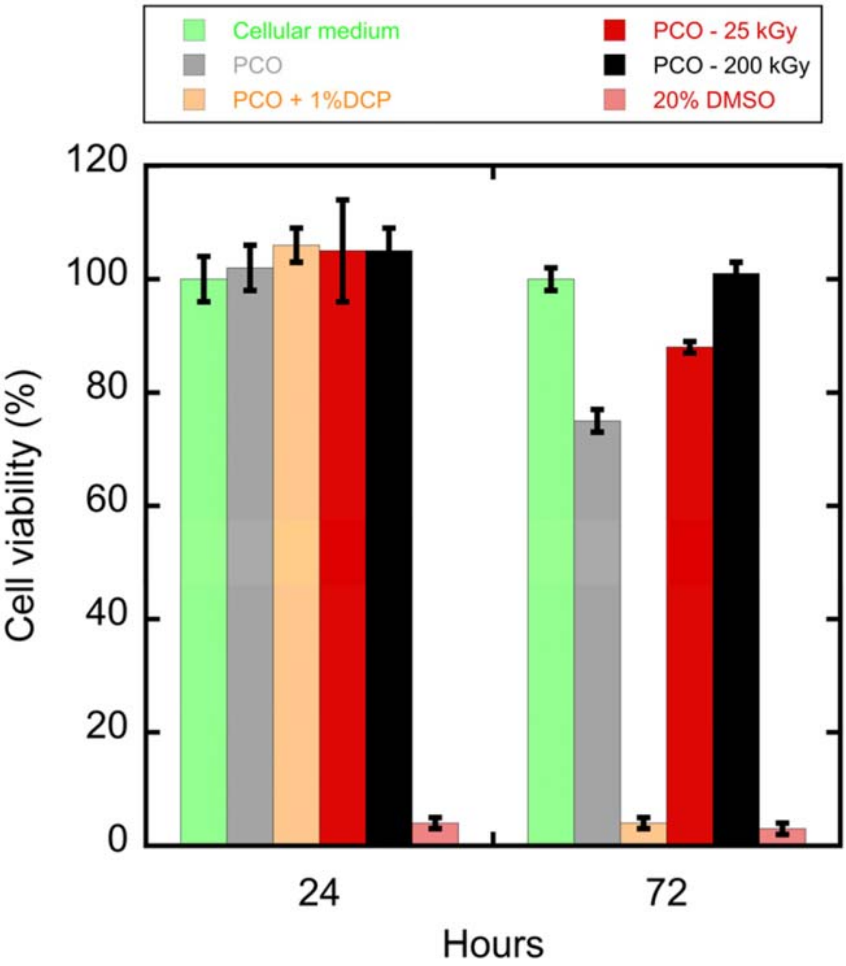

Figure 1 Cytotoxicity assay results according ISO standard 10993-5. Cell viability after 24 and 72 h exposure to extract medium of the different test specimens (PCO, PCO11% DCP, PCO-25, and PCO-200), negative control (cellular medium) and positive control (20% DMSO).

3.3 Shape memory properties

For the sake of the study of the shape memory properties, a cyclic thermomechanical experiment was performed in the stress-controlled mode as in previous studies [3.22]. As above the T_m it flows like a viscous liquid, non-irradiated PCO sample does not have shape memory behavior and was therefore excluded from TMA experiments. Strip-shaped samples (4 mm x 1.5 mm x 20 mm) were cut from the irradiated PCO sheets. TMA was conducted on a Mettler Toledo DMA-1 in temperatures ranging of 30–80 °C at a 4 °C min^{-1} heating rate. The temperature range was selected taking into account the maximum melting peak (T_m) from calorimetric analysis listed in Table 1 (around 55 °C), since this is defined as the transition temperature (T_{trans}) at which shape memory effect starts. The margin of error for extension measurements is deemed to be null as the technical resolution is 2 nm and the sensitivity is 30 nm. Extension (increase in the sample length) versus temperature was recorded (Figure 2).

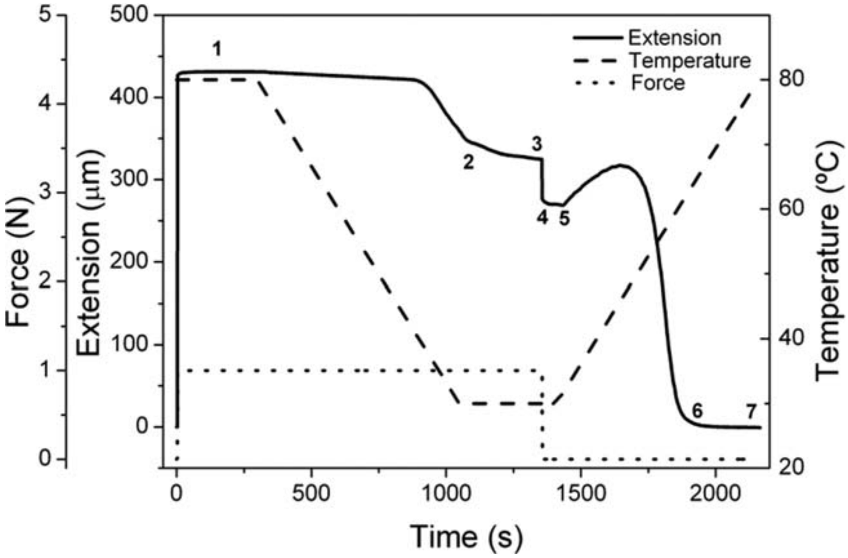

Figure 2 Extension, temperature and force of the cyclic thermomechanical experiment.

As shown in Figure 2, first, departing from the original shape of the samples the temperature was fixed at 80 ºC in order to allow relaxation of the polymer chains. After this, a 1 N force was applied and maintained for 5 min. The length of the sample at this point is named extension 1 (see Table 2).

Then, the temperature was decreased (4 ºC min^{-1}) until 30 ºC were reached, causing a reduction in the length of the samples (extension 2). During this cooling process, crystallization occurs. The crystalline phase is stiffer and more stable than the amorphous one [3.23]. So, as the irradiation dose increases, crystallinity is reduced, resulting in a higher thermal contraction (lower values of extension 2, see Table 2).

The temperature was maintained at 30 ºC for 5 min and deformation is stabilized (extension 3). Next, the applied force was ceased to fix the temporary shape (extension 4). In shape memory semicrystalline systems, fixation occurs by cause of the strong mechanical "locking" of the crystalline phase.

The samples are maintained at 30 ºC without force by 1 min (extension 5). Finally, the temperature was increased (4 ºC min^{-1}) until 80 ºC and as T_{trans} (or T_m) was reached, recovery process takes place and recovered shape was obtained due to the entropic elasticity of the samples.

Results of Table 2 shows that the deformation at different points (Extensions 1 – 5) depends on the crosslink density. A higher irradiation dose originates a higher crosslinking density. Due to the strength and resistance to deformation caused by the crosslink density, a higher crosslinking density derives in a shorter extension. This decrease of extension is also brought up above T_{trans} as shown in Table 3.

Sample	Ext.1 (μm)	Ext.2 (μm)	Ext.3 (μm)	Ext.4 (μm)	Ext.5 (μm)
PCO-25	436.0	422.4	388.0	308.1	299.0
PCO-50	437.9	417.7	392.6	290.8	278.8
PCO-75	431.0	359.4	324.7	276.6	270.0
PCO-200	426.0	320.2	285.8	221.5	213.6

Table 2 Extension values for all samples at different steps of the thermomechanical cycle. The error is ± 0.1 μm in all cases.

In Table 3 final recovery temperatures (T_f), the final extension (remnant extension, extension 6), and extensions at 80 ºC, the final temperature of the TMA test (extension 7) are highlighted. Moreover, the fixity ratio R_f and shape recovery ratio R_r are also provided. At this point, it is important to define some usual concepts of cyclic-mechanical tests relating shape-memory properties. In Figure 2, ε_m is the strain before the load was released (Point 1 – extension 1), ε_u is the strain obtained after releasing the applied load (Point 4 – extension 4), and ε_p is the final strain after heating and without load, that is, after maximum recovery of the deformation (Point 6 – extension 6). With this, we have:

$$R_f(\%) = \left(\frac{\varepsilon_u(N)}{\varepsilon_m(N)} \right) x100$$

$$R_r(\%) = \left(\frac{\varepsilon_m(N) - \varepsilon_p(N)}{\varepsilon_m(N) - \varepsilon_p(N-1)} \right) x100$$

where N is the number of cycles. The strain fixity ratio, R_f, quantifies the ability to fix a mechanical deformation ε_m resulting in a temporary shape $\varepsilon_u(N)$. The strain recovery ratio R_r quantifies the ability to restore the mechanical deformation of the permanent shape $\varepsilon_p(N)$ after application of a certain deformation, ε_m. For an ideal shape memory recovery, R_f and R_r should be 100%. From results of Table 3 it is deduced that the shape fixity ratio R_f decreases as radiation dose increases, and that the recovery ratio R_r is higher when crosslink density grows.

Sample	R_f (%)	T_f (°C)	Ext.6 (μm)	R_r (%)	T (°C)	Ext.7 (μm)	R_r (%)
PCO-25	70.66 ± 0.03	65.7	4.5 ± 0.1	98.97 ± 0.02	80.0	4.2 ± 0.1	99.04 ± 0.02
PCO-50	66.41 ± 0.03	65.5	3.1 ± 0.1	99.29 ± 0.02	80.0	2.4 ± 0.1	99.45 ± 0.02
PCO-75	64.18 ± 0.03	67.3	1.0 ± 0.1	99.77 ± 0.02	80.0	0.0 ± 0.1	100.00 ± 0.02
PCO-200	52.00 ± 0.03	60.3	0.0 ± 0.1	100.00 ± 0.02	80.0	0.0 ± 0.1	100.00 ± 0.02

Table 3 Values obtained in the recovery process for all samples.

In summary, an increment in radiation dose involves a drop in crystallinity and related shape memory transition temperature (Table 1). In this way, shape fixity ratio R_f decreases as radiation dose increases due to the lack of chain mobility and crystallization process, and recovery ratio R_r is higher when crosslink density grows from enhanced rubbery elasticity (Tables 2 and 3).

The cyclic thermomechanical response of all the samples is shown in Figure 3 and the shape memory cycles are plotted in Figure 4. It is important to mention that PCO-75 sample exhibits a weird behavior. During the radiation of the samples several processes take place simultaneously (crosslinking, chain scission…), and how the radiation affects the distribution and size of the crystallites in the PCO samples is not exactly known. The peak at about 1700 sec is directly related with these crystallites. The mentioned effect may have affected in a different way the PCO-75 sample, differencing the trend of the peak from the other samples. In any case, shape memory behaviour seems to be unaffected seeing the results shown in Table 3.

The actual quantitative experiments highlights that PCO-75 and PCO-200 samples have a total shape recovery (100%) at extension 7, which is in agreement with previous qualitative results [3.15]. Furthermore, PCO-25 and PCO-50 samples exhibited a “partial” shape recovery in the previous study [3.15]. In the present experiment these samples neither arise the 100% of the recovery (99.04% and 99.45% with an error of 0.02% at extension 7).

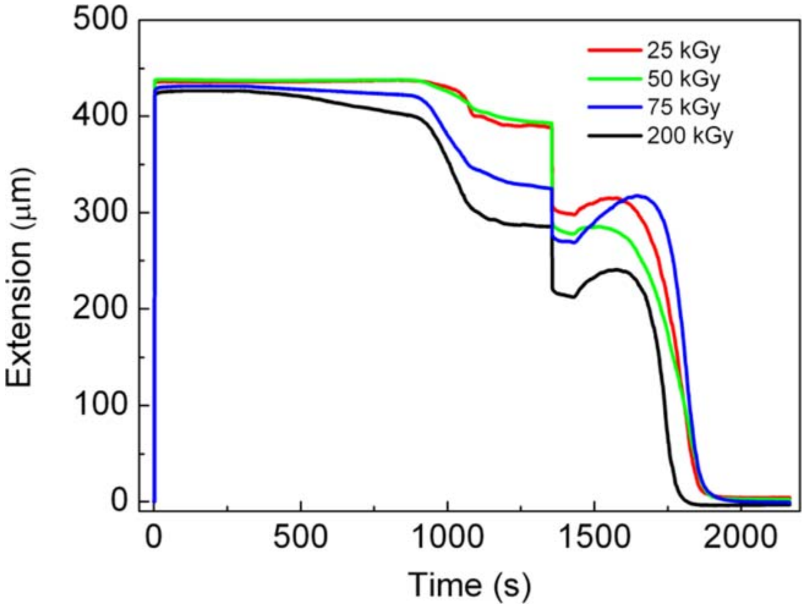

Figure 3. Cyclic thermomechanical response of irradiated PCO samples showing extension for each sample as a function of time, illustrating the shape programming and recovery for the first cycle.

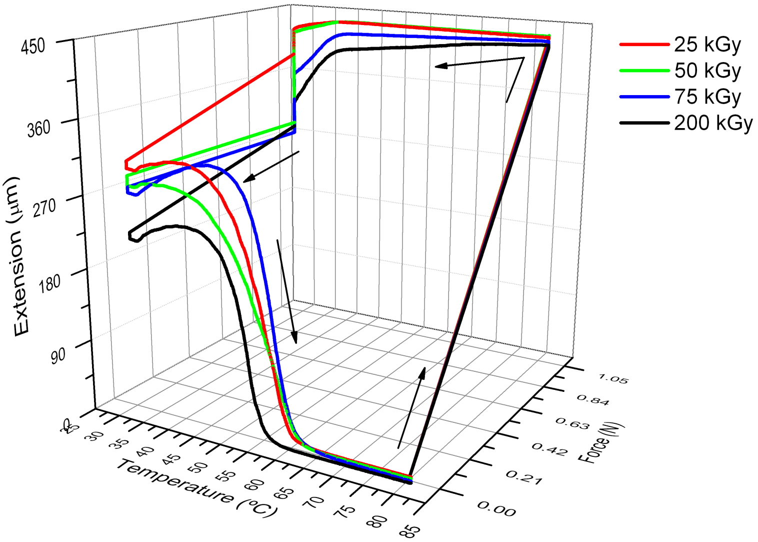

Figure 4 Three-dimensional thermomechanical cycle to evaluate the shape memory properties for irradiated PCO samples (first cycle).

It has been recently demonstrated that the radiation crosslinking generates an increase of the gel fraction of these polymers. Figure 5 shows the linear correlation between the gel fraction [3.15] and the shape recovered after the first cycle obtained by TMA. It is important to mention that this linear correlation of the gel fraction and the shape recovery ratio arises in a small interval (around 1% of the recovery). Of course, this relation is not linear if we include the not irradiated PCO sample (0% gel fraction, no shape memory). Only irradiated samples (samples with shape memory) exhibit this linear correlation. The resolution is good enough to show and support the differences in the recovery ratio between the samples as the interval is 50 times larger than the error.

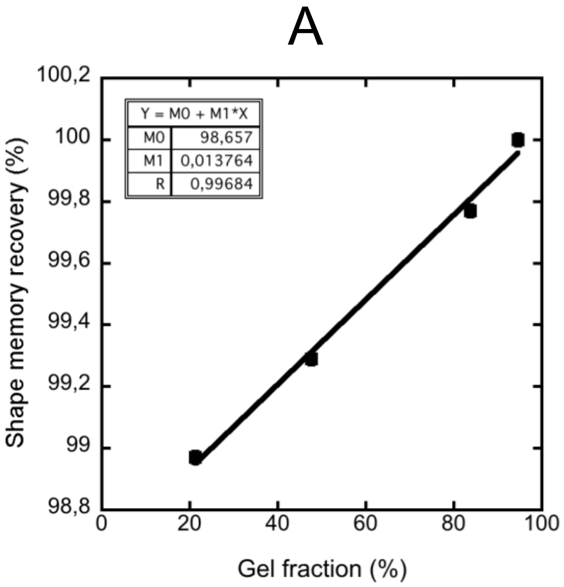

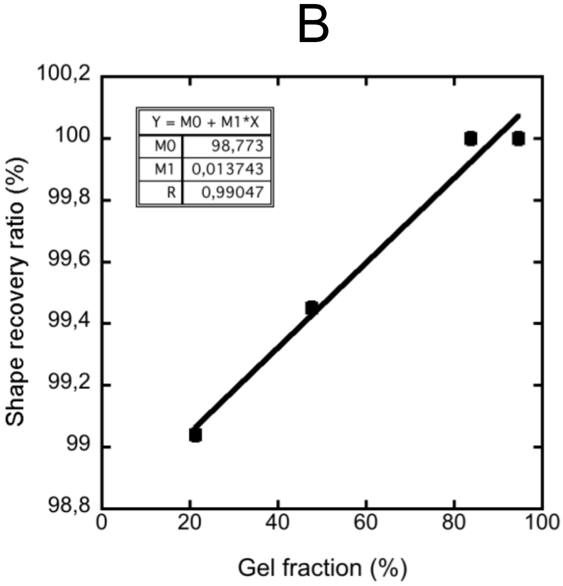

Figure 5 Linear correlation (R=0.99) of the percentage of the shape recovered after the first shape memory recovery cycle at extension 6 (A) and at extension 7 (B), and the gel fraction of the samples measured in a previous study [3.15]. Note that the error of the recovery is ± 0.02%.

3.4 Free volume hole sizes

The PALS equipment utilized and the measurement of the free volume void size is described in the first chapter of the present thesis. The source employed was the T1 one (more information of the positron source is available in section 1.1). The installed temperature controller was performed to measure in the 15 ºC – 80 ºC temperature range in order to measure the o-Ps lifetimes both above and below the T_m of the polymer samples. The measured mean o-Ps lifetimes versus temperature is shown in Figure 6. As expected, the o-Ps lifetimes increase with increasing temperature. For example, the mean o-Ps lifetime of the non-irradiated PCO increases from 2.55 ± 0.02 ns at 10 °C to 2.77 ± 0.01 ns at 80 °C; in the case of the sample irradiated at 200 kGy, this value increases from 2.72 ± 0.02 ns at 10 °C to 2.84 ± 0.02 ns at 80 °C.

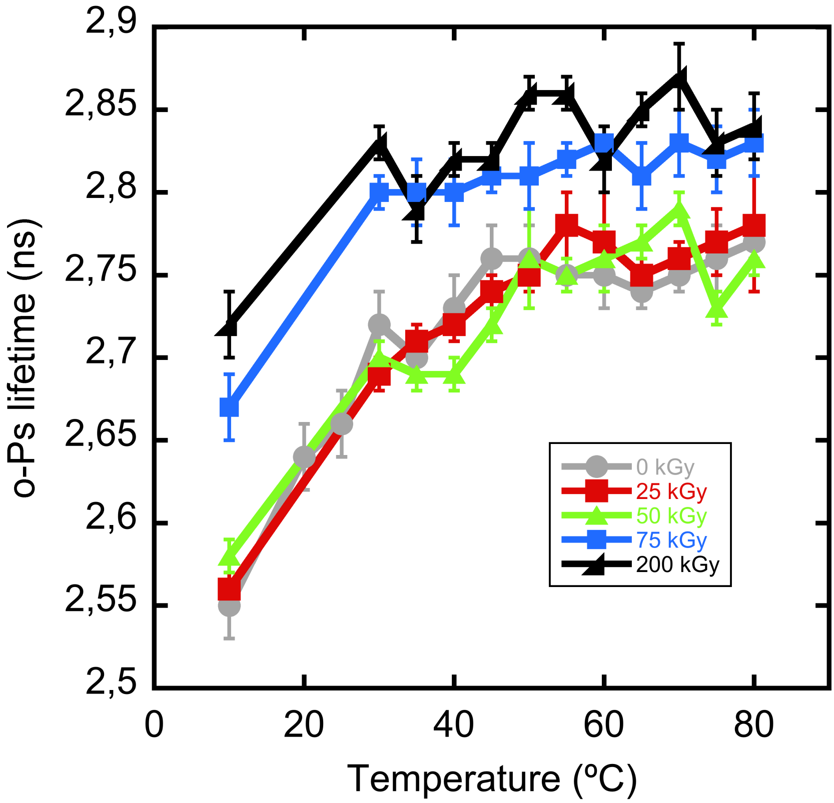

Figure 6 Temperature dependence of the mean ortho-Positronium lifetime (o-Ps lifetime) obtained by PALS for gamma-irradiated PCO samples at different doses: 25 kGy (red), 50 kGy (green), 75 kGy (blue), 200 kGy (black) and a control PCO sample (0 kGy - grey). A gap is highlighted between samples with partial shape recovery (red and green) and total shape recovery (blue and black).

3.5 Relation between free volume and shape memory properties

As mentioned before, in gamma irradiated shape memory polymers, the recovery process is related to crosslinking density and associated rubbery elasticity. As a consequence, higher crosslink density leads to higher recovery ratios, i.e. lower values of extensions 6 and 7.

Interestingly, a gap is highlighted between samples with partial shape recovery (red and green) and with total shape recovery (blue and black in Figure 6). At 10 ºC, the mean o-Ps lifetime of the sample irradiated at 200 kGy (total shape recovery) is around 6% larger than the sample irradiated at 25 kGy (partial shape recovery). At 80 ºC, this value is around 2.5% bigger for the sample irradiated at 75 kGy (total shape recovery) compared with the sample irradiated at 50 kGy (partial shape recovery). So, as can be observed, higher free volume hole sizes imply improved shape memory recoverability. A possible explanation for this might be that molecular segments could move easily due to the larger free volume space between them, improving the recovery to the original shape.

The mean free volume hole size of the samples obtained by PALS at different temperatures versus the gel fraction inside samples (wt%) obtained in García-Huete et al. [3.15] is shown in Figure 7. The mean free volume hole size increases when increasing the gel fraction. A similar trend is found when comparing the mean free volume hole size of the samples obtained by PALS at different temperatures versus the percentage of the shape recovered after the first shape memory recovery cycle obtained by TMA (Figure 8).

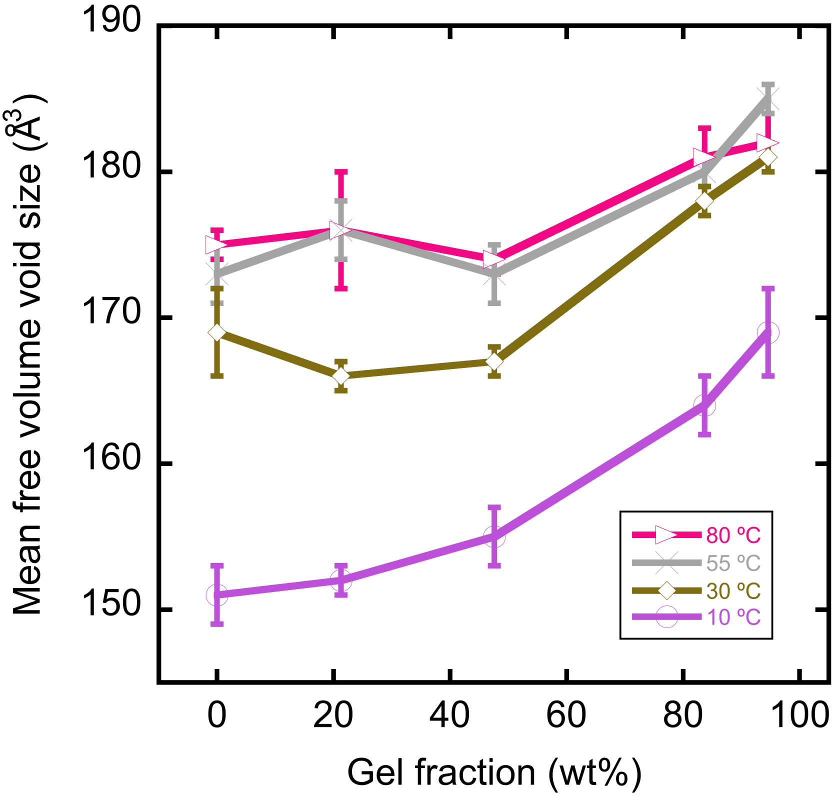

Figure 7 Mean free volume hole size of the samples obtained by PALS at different temperatures versus the gel fraction inside samples (wt%) obtained in a previous study [3.15].

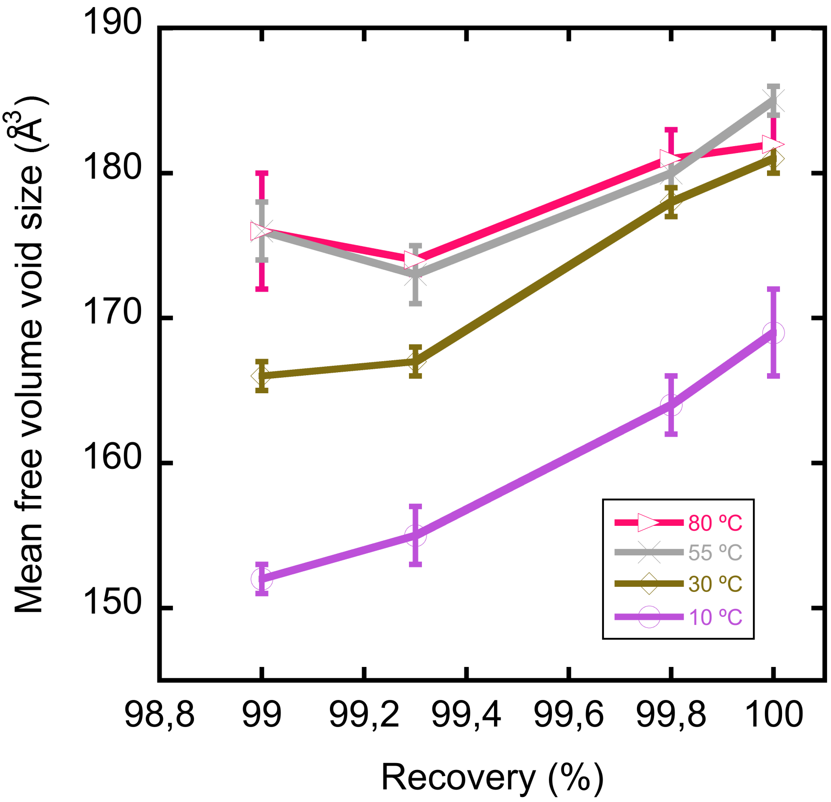

Figure 8 Mean free volume hole size of the samples obtained by PALS at different temperatures versus the percentage of the shape recovered (Recovery (%)) after the first shape memory recovery cycle. Note that error bars of the recovery (± 0.02%) are not shown as they are smaller than the corresponding symbol.

Considering the thermo-mechanical properties and the associated shape memory response, the gel fraction above 20% and the shape recovery after the first cycle are linearly correlated, as shown in Figure 5. Furthermore, as the gel fraction was previously attributed to the radiation crosslinking [3.15], the gamma radiation crosslinking can be considered as a rational parameter to design and control a macro-scale shape recovery.

An increase in the gamma radiation dose leads to a growth both in the gel fraction and in the shape recovery percentage. The underlying physicochemical mechanism can be explained as follows: to begin with, the mean free volume hole size increases with the radiation dose. The crosslinking increases the free volume hole sizes due to the insufficient PCO chain packing. In this way, the PCO chains can move faster [3.15] and efficiently to strain for the shape recovery when the temperature increases, as shown in Figures 6, 7 and 8. Furthermore, Figure 6 highlights an abrupt increase in the ortho-positronium lifetime (free volume hole size) between the samples with partial macroscale recovery (50 kGy) and total macroscale recovery (75 kGy).

It can be concluded that the free volume hole size is a (sub)nanoscale parameter directly affecting the shape memory properties of these SMPs, although the general link between the molecular scale free volume holes and the micro/macroscale shape memory properties in polymers needs to be confirmed in other SMPs.

3.6 Conclusions

PALS measurements highlight an increase in size of the (sub)nanoscale free volume holes caused by gamma irradiation in PCO samples that facilitates the movement of polymer chains, enhancing the recovery to the original macroscopic shape. In this way, results suggest a physicochemical link between the size of the free volume holes and shape memory properties of the gamma irradiated polycyclooctene (PCO).

It is demonstrated that the gamma irradiated polycyclooctene (PCO) samples are non-cytotoxic; this is a first step towards developing biomedical applications based on these shape memory polymers.

CHAPTER 4

THE ROLE OF THE FREE VOLUME HOLE SIZE IN TISSUE ENGINEERING MATERIALS

There exists a need for tissue replacement: today, the 20% of people older than 65 in developed countries will benefit from organ replacement technology [4.1]. As transplantations are limited by the number of compatible donors, tissue engineering rises up as an alternative strategy which seeks to regenerate damaged tissues. Tissue engineering combines materials science and biology for developing functional substitutes of tissues and organs; porous 3D scaffolds are used as template and seeded with cells (stimulated by different strategies as growth factors) in order to regenerate the damaged tissue [4.2]. Among others, skin, bladder, airway, bone or cartilage tissue-engineered constructs have been successfully used in patients by following this strategy [4.3].

The number of living cells per gram of tissue in the human body is around 10^9 [4.4]. This amount of cells is massive: there are more cells in our body than stars in our galaxy. To function appropriately, all cells need a certain quantity of oxygen and nutrients. The Thiele modulus [4.5], S, has been utilised for tissue engineering and defined as a dimensionless ratio of consumption to supply of nutrients. In this way, when S>>1, cells consume more than can be delivered, when S<<1 the nutrient supply is greater than demand and if S=1 the supply equals the demand of nutrients.

$$S = \frac{k\rho x^2}{DC_o}$$

Being k the cell nutrient uptake rate constant [mol/sec/cell], ρ the cell density in the scaffold [cells/cm^3], x the distance from nutrient source (bloodstream), D the nutrient diffusivity in the scaffold [cm^2/sec] and C_o the nutrient concentration at source [mol/cm^3]. In Figure 1 it is shown a scheme of the nutrient concentration versus the distance.

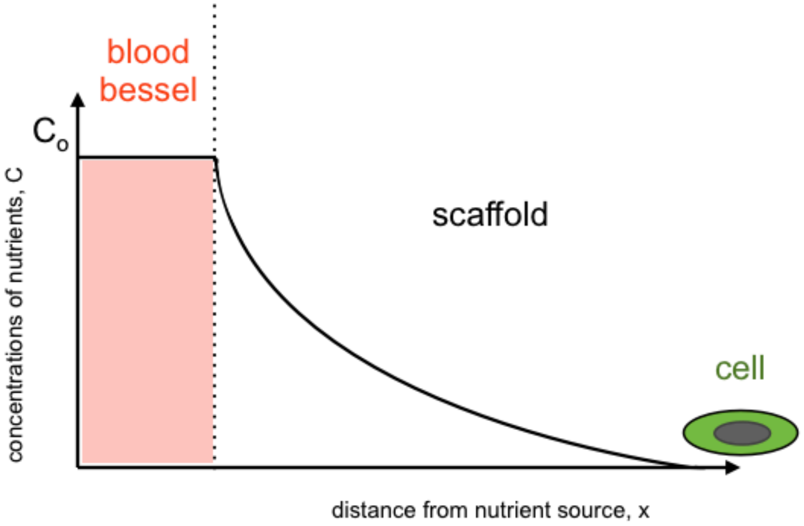

Figure 1 Concentrations of nutrients versus distance from nutrient source in scaffolds.

Therefore, the diffusivity of the nutrients within the scaffold plays a key role in the success of cell proliferation. In fact, the diffusion of nutrients within the scaffold has been previously identified as one of the major problems when designing a scaffold for tissue engineering applications. There are scarce physical parameters of the scaffold for tissue engineering that can be used to link molecular diffusion (or to rationally control the diffusivity); unfortunately, the diffusion process itself remains unclear. In this context and in spite of its satisfactory outcome to describe molecular diffusion in polymeric systems, surprisingly, free volume theory has never been employed in the context of tissue engineering materials. Free volume is the dominant parameter determining the diffusion rate of molecules. As explained in the first chapter of this thesis, the sub-nanoscale free volume holes collectively form this free volume in polymers. In 2009 Lv et al. [4.6] published an interesting method to calculate the free volume available for molecular transport from PALS measurements. This strategy has potential applications in the prediction of diffusivities for tissue engineering applications.

Chitosan is a biopolymer extensively used as 3D scaffold for new osseous tissue formation because it promotes cell growth and allow osteoconduction (it is biodegradable, biocompatible, antibacterial, bioadhesive and can be molded to have interconnected high porosity) [4.7-4.11]. Nevertheless, the weak mechanical strength and the loss of structural integrity under wet conditions of chitosan restrict the use in bone tissue engineering [4.12,4.13]. Fortunately, chitosan may be combined with other materials in order to enhance its strength and cell adhesion [4.14]. Furthermore, the appropriate addition of carbon nanotubes (CNTs) to chitosan matrix improves many of its physical and chemical properties, including mechanical properties for bone tissue engineering applications [4.13,4.15-4.17]. Previous studies consider the improvement of mechanical strength of chitosan matrix by CNTs incorporation as nanometer-scale reinforcement. However, nano-level mechanical and structural properties of chitosan/CNTs scaffolds remain unknown.

The aim of the work in this chapter is to study the effect of CNTs addition in the free volume hole size of chitosan in order to calculate the effect in the ratio of free volume holes available for diffusion of nutrients (in this case oxygen and glucose, essential for cells). We further investigated the nanostructure and nanomechanical properties of chitosan and chitosan/CNTs nanocomposites. To that end, we combined several techniques. Using PALS, we characterized the sub-nanometer sized free volume holes in chitosan and chitosan/CNTs scaffolds under physiological conditions. We measured the local Young´s modulus of the samples under wet conditions at the nanoscale by force spectroscopy. We used SEM and AFM imaging to characterize the porosity of the scaffolds and the interaction between chitosan and CNTs, respectively.

4.1 Materials and sample preparation

4.1.1 Chitosan and chitosan/CNTs solutions preparation

The sample preparation was carried out by the author of this thesis at the Department of Physics in the University of Oxford under the supervision of Prof. S. Contera. The author was supported in part by a previous work by Loïc Bugnicourt at the Department of Physics in the University of Oxford, which has been very beneficial to this section of the study (specifically, the acid treatment of carbon nanotubes and AFM imaging).

Medium molecular weight chitosan (190 kDa – 310 kDa, 75 – 85 % deacetylated) and single-walled carbon nanotubes (SWNTs) with a diameter size of 0.7 – 1.1 nm and a length of 300 – 2300 nm (mode 800 nm) (both from Sigma Aldrich, USA) were utilized. Acid-treatment of SWNTs was carried out by mixing 12.7 mg of SWNTs, 10 ml of sulfuric acid (Acros Organics) and 3.333 ml of nitric acid (Acros Organics) in a SFE 590/1 029050 ultrasound bath sonicator (Ultuntreatedave Limited, UK) at 60 °C for 1 h. After this, the acid was filtered with a polytetrafluoroethylene (PTFE) filter for 24 h. Ultrapure water and 1 M NaOH was added to neutralize the acid on the nanotubes. The obtained solution was inserted in the ultrasonicator bath for 1 h. The resulting SWNTs had a length determined by AFM imaging of 20 – 475 nm with a mean length of 78 nm.

50 mM sodium acetate buffer (Sigma Aldrich) containing 1% (vol) of acetic acid was prepared. The pH was adjusted to 4, using a 1 M NaOH (Sigma Aldrich) solution. 100 mg of chitosan powder (Sigma Aldrich) were added to 10 ml of the buffer in a round-bottom flask. The mixture was stirred with a magnetic shaker for 3h at 45 G. Next, an ultrasonicator bath (SFE 590/1 029050 Ultuntreatedave, UK) was employed for 20 min. In order to remove undissolved chitosan, a centrifuge (5415D Eppendorf, Germany) was used for 5 min at 16,600 G. The supernatant was used for preparing 3 different samples: (i) 0.5 % wt chitosan solution was prepared by diluting with buffer the original solution. The obtained solution was stirred for 1 h at 33 G and then untrasonicated for 30 min. (ii) 0.5 % wt chitosan solution containing 0.25 mg/ml acid-treated SWNTs. The solution was stirred for 1 h at 33 G and transferred to an ultrasonicator bath for 30 min. (iii) 0.5 % wt chitosan solution containing 0.25 mg/ml "untreated" SWNTs was prepared. The solution was stirred for 1 h at 33 G and transferred to an ultrasonicator bath for 30 min. A VCX 400 probe ultrasonicator (Sonics & Materials Inc. Vibra Cell (USA)) was used to disperse the SWNTs. The power was set at 100 W for 1 h, until the sample was homogenized, in pulsing mode (0.8 s on, 0.2 s off). Finally, residues were removed by centrifuging the solution for 20 sec at 9,300 G.

4.1.2 Sample preparation for AFM imaging

For imaging acid-treated SWNTs/chitosan complexes, a mixture of 1 ml (1 mg/ml) acid-treated SWNTs/chitosan, with 2 ml of chitosan solution (50 mM acetate/acetic acid buffer, pH 4) was prepared by shaking, resulting in good dispersion of the SWNTs. For imaging, the samples were further diluted to 0.005 mg/ml. Then, a 0.5 µl drop was deposited on mica, rinsed with ultrapure water and air-dried. For images of untreated SWNTs/chitosan interactions 1 mg of untreated, dry, SWNTs were mixed with a 2 ml of chitosan solution by ultrasonication (100 W for 1 h, pulse mode 0,8 s on 0,2 s off, and maintained at 5 °C). For imaging, the samples were further diluted to 0.005 mg/ml. Then, a 0.5 µl drop was deposited on mica, rinsed in ultrapure water and air-dried.

4.1.3 Scaffold fabrication

The scaffolds were fabricated (using the solutions prepared by this author at the Department of Physics in the University of Oxford) at the Biophysics Unit UPV/EHU - CSIC (with the assistance of Ruben Sanchez-Eugenia) and the Nuclear Techniques Laboratory at the UPV/EHU (with the assistance of Iraultza Unzueta).

Three samples of 200 µl of each solution were deposited in a cylindrical mould. The samples were pre-frozen in dry ice at -65 ± 5 °C for 30 min. Next, the samples were freeze-dried at -65 ºC under vacuum at 70 mTorr (VirTis 420617, SP Industries Inc., USA). The resulting sponges were neutralized in a 1 M NaOH solution for 5 h. Then, the scaffolds were rinsed 4 times and incubated for 15 min in ultrapure water. Finally, the samples were dried over 48 h under vacuum at 10 mTorr using a desiccator (Kartell, Italy) connected to a vacuum pump (A65201903 Edwards, UK).

4.2 Scanning Electron Microscopy (SEM)

SEM measurements were performed with the assistance of Maite Goiriena-Goikoetxea and SGIker staff at the Faculty of Medicine and Ondontology of the UPV/EHU.

The scaffolds samples were fixed by a double coated, 8 mm-wide, carbon conductive tape from Ted Pella, Inc. (USA) and sputter-coated with a gold layer. Images were obtained with a S4800 SEM from Hitachi (Japan). Figure 2 shows (A) chitosan sponges, with few and poorly connected pores. (B) Acid-treated SWNTs/chitosan scaffolds with a wide distribution of interconnected pores $\geq 150\ \mu m$, which is appropriate for bone tissue engineering applications due to the suitable size of the pores, big enough for the proper motion of cells within the scaffold. (C) Untreated SWNTs/chitosan scaffolds with a wide distribution of interconnected pores $\leq 150\ \mu m$.

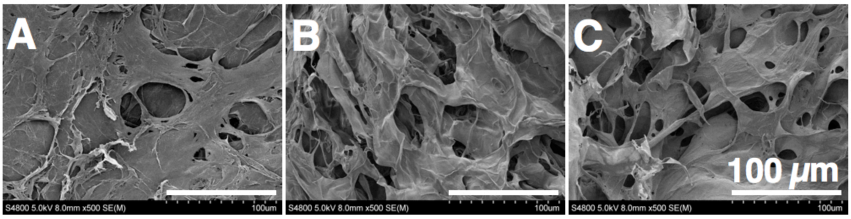

Figure 2 SEM images of (a) chitosan, (b) chitosan/acid-treated SWNTs, and (c) chitosan/untreated SWNT nanocomposite scaffolds. The scale bar is 100 μm in all the images.

4.3 Positron Annihilation Lifetime Spectroscopy (PALS)

In order to perform the PALS measurements under physiological conditions, the sponges were hydrated with a 10 mM HEPES buffer containing 154 mM NaCl and pH 7.4 at 37 °C (human body temperature). The PALS equipment utilized and the measurement of the free volume void size is described in the first chapter of the present thesis. The assistance of David Merida was helpful at this point. We utilized the positron source T1, described in section 1.1.

$\sim 2.5\times10^6$ counts were collected for each positron lifetime spectrum. Measured o-Ps lifetime distributions are plotted in Figure 3. The obtained o-Ps mean lifetime are 1.87 ± 0.02 ns for chitosan, 1.80 ± 0.06 ns for acid-treated CNTs/chitosan, and 1.93 ± 0.02 ns for untreated CNTs/chitosan. From this data and using the Tao-Eldrup equation (see Chapter 1) we calculate the mean free volume void size and distributions shown in Table 1. The values of the mean free volume void size and distribution within the acid-treated SWNTs/chitosan sample are respectively 6% and 28% shorter than in chitosan alone; contrarily, for the untreated SWNTs/chitosan sample are respectively 6% and 20% larger than in chitosan.

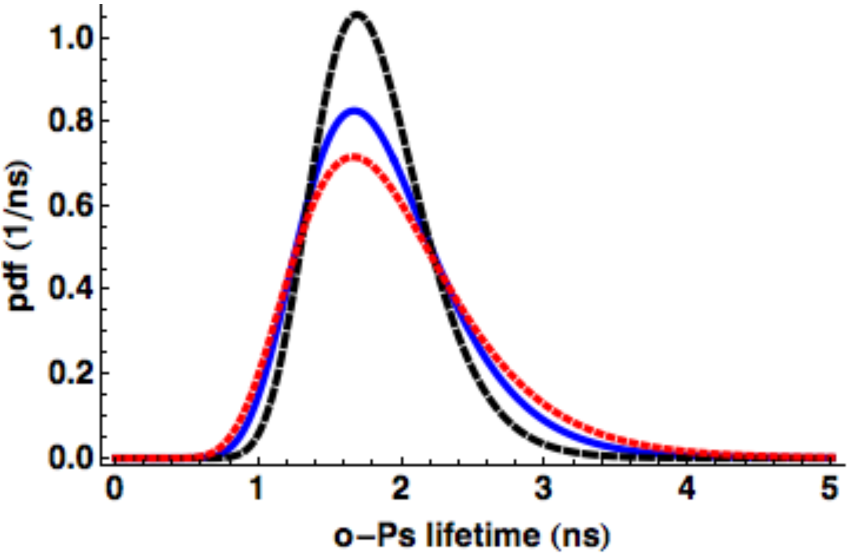

Figure 3 Probability density functions (pdf) of lognormal distributions of measured ortho-Positronium (o-Ps) lifetimes corresponding to chitosan (blue), chitosan containing acid-treated SWNTs (dashed, black) and chitosan with untreated SWNTs (dotted, red).

Sample	$\langle V_f \rangle [\text{Å}^3]$	$\sigma [\text{Å}^3]$
Chitosan	85 ± 2	50 ± 2
C/AT-SWNTs	80 ± 5	36 ± 2
C/U-SWNTs	90 ± 2	60 ± 2

Table 1 Mean free volume hole size ($<V_f>$, Å^3) and distribution (σ, Å^3) obtained by PALS in chitosan, chitosan containing acid-treated SWNTs (C/AT-SWNTs) and chitosan with untreated SWNTs (C/U-SWNTs).

By using the free-volume probability density function from PALS (see Figure 3), V_{pdf} (V_f), the cumulative distribution of free volume holes effective for transport C was calculated employing the following relationship [4.6]:

$$C\left(V_f \geq V_c\right) = \int_{V_c}^{V_{f,max}} V_{pdf}\left(V_f\right) dV_f$$

where $V_{f,max}$, is the largest free-volume hole of the material and V_c is the hole critical volume. Following the free volume theory, at ordinary energies the transport of a molecule in a polymeric or fluid system is regulated by the free volume: mass transport of small molecules happens if a free volume larger than certain critical size exists next to the molecule [4.18]. Free-volume holes smaller than this critical volume do not contribute to diffusion. Using the Bondi´s group contribution [4.19] (see Chapter 1), the critical hole volume of the molecule can be estimated as V_c = 1.3 V_W, where V_c is the critical hole volume equal to the specific volume at absolute zero of the molecule, 1.3 is a factor assumed to be a universal constant effective for all groups and structures, and V_W is the van der Waals volume of the diffusing molecule. Although it is clear that the obtained data from this assumption should be treated cautiously due to its *naïf* hole description mechanism (i.e., the model does not consider molecular vibrations increasing with the temperature), this model is widely used because, even though in a preliminary manner, it sheds light on the molecular diffusion via free volume quantitatively. By using the well known van der Waals radius and bond length of oxygen and the molar mass and the density of the glucose, we calculated the critical hole volumes $V_{C,O2}$ ~29.94 $Å^3$ and $V_{C,C6H12O6}$ ~252.55 $Å^3$. Once calculated the critical hole volumes for oxygen and glucose transport, from measured free volume hole size distributions plotted in Figure 4, the cumulative distributions of holes effective for oxygen and glucose transport were calculated (Table 2). The results highlight how does the incorporation of carbon nanotubes alter the available free volume holes for diffusion within the hydrated chitosan scaffold. As an example, the percentage of the free volume available for oxygen diffusion increases a 3% by incorporation of short acid-treated SWNTs to the chitosan matrix. Another example: incorporation of long, more hydrophobic, untreated SWNTs, duplicates the percentage of holes available for the transport of glucose.

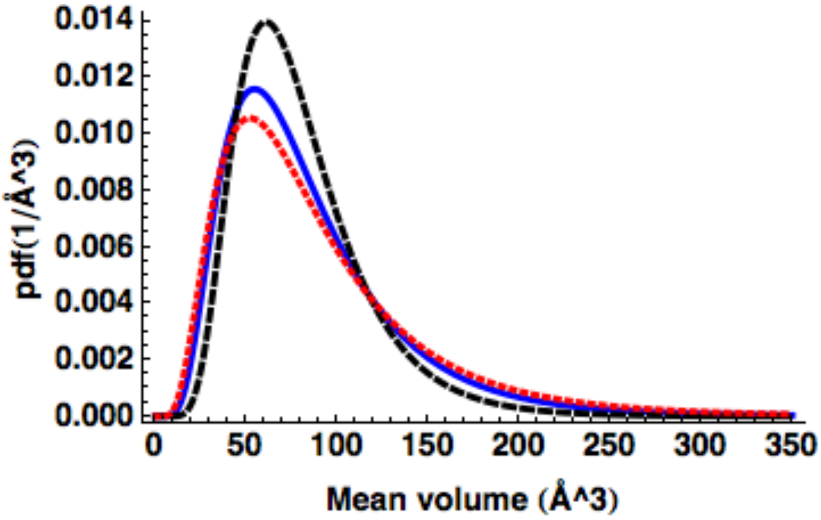

Figure 4 Probability density functions (pdf) of free-volume hole size lognormal distributions corresponding to chitosan (blue), chitosan containing acid-treated SWNTs (dashed, black) and chitosan with untreated SWNTs (dotted, red).

Sample	O_2 [%]	$C_6H_{12}O_6$ [%]
Chitosan	95.0 ± 0.7	1.2 ± 0.4
C/AT-SWNTs	98.1 ± 0.7	0.2 ± 0.2
C/U-SWNTs	93.5 ± 0.8	2.3 ± 0.3

Table 2 Estimation of the percentage of free volume holes available for oxygen (O_2) and glucose ($C_6H_{12}O_6$) diffusion obtained by PALS in chitosan, chitosan containing acid-treated SWNTs (C/AT-SWNTs) and chitosan with untreated SWNTs (C/U-SWNTs) hydrated scaffolds.

In Polymer Physics the widespread concept of free volume has been successfully related to the diffusion of small molecules within the polymeric matrix [4.20]. As demonstrated in this chapter, the free volume hole size can be considered as an experimental parameter related with diffusion of nutrients for cells in scaffolds for tissue engineering too. The author of this thesis considers this suggestion important because it can lead to a diffusion rational design in materials for tissue engineering, drug delivery and 3D culture applications. Future experiments connecting the free volume with nutrient transport diffusion in other scaffolds are suggested to validate this strategy.

4.4 Atomic Force Microscopy (AFM)

Static force spectroscopy measurements and AFM imaging were performed using a MFP-3D AFM from Asylum Research (USA).

4.4.1 AFM imaging

The interaction of individual SWNTs with chitosan macromolecules was studied using AFM imaging with an operation mode of amplitude modulation (AM-AFM). For imaging in air Si, Olympus OMCL-AC240TS cantilevers were used and for imaging in liquid, SiN, Olympus OMCL-TR800PSA cantilevers were utilized.

Figure 5 (A) and (B) show the interaction of individual molecules of chitosan with 2 acid-treated SWNTs of different length; chitosan molecules seem to wrap around the SWNTs, dispersing them. This fact could explain PALS results: as the SWNTs are tightly wrapped, the packing increases, reducing the size of free volume holes. Figure 5 (C) shows a height image of longer, untreated SWNTs interactions with chitosan in air. Raw SWNTs are *zipper-up* together by chitosan biomolecules, originating the alignment of the SWNTs in parallel bundles. Unlike the acid-treated SWNTs, untreated SWNTs are not soluble *per se*. In this case, the solubility of raw SWNTs is caused by sonication with chitosan. This process may induce stronger hydrophobic interactions. The lack of defects at the surface of SWNTs would obstruct the formation of electrostatic interactions with chitosan chains, originating the increase of the free volume reflected by PALS.

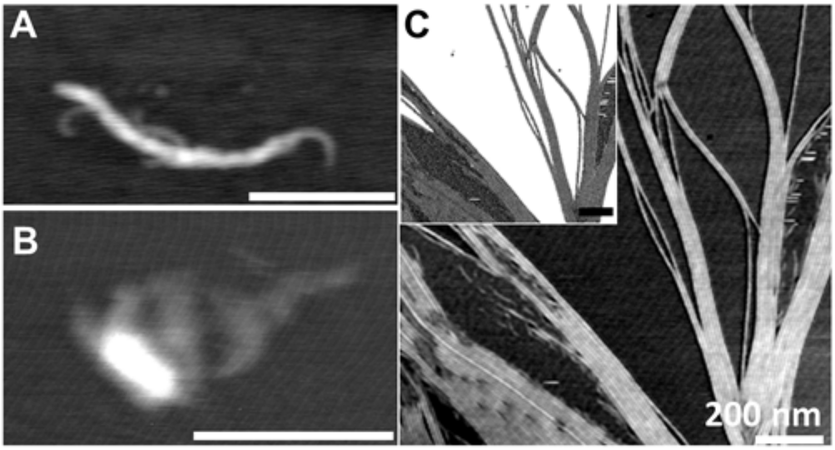

Figure 5 AFM images of chitosan-SWNTs complexes. (A,B) AM-AFM height images of 2 individual acid-treated SWNT interacting with chitosan. The height scale is 0 - 2.5 nm (grey scale from back to white). (C) AM-AFM height image of the interaction of longer untreated SWNTs with chitosan molecules, the height scale is 0 – 2 nm. In the inset a second eigenmode phase image in dual-mode shows mechanical properties contrast between the different materials (mica white, SWNTs lighter grey, chitosan darker grey). The scale bar is 200 nm in all the images.

4.4.2 Force spectroscopy

Force versus distance measurements were conducted after thermal equilibration, under physiological ionic strength conditions, using the same buffer as for PALS experiments. 3 µl of this HEPES buffer was deposited on freshly cleaved mica (Agar Scientific, United Kingdom); after 5 min, the sample was deposited and hydrated with 200 µl of the same buffer. SiN cantilevers (OMCL-RC800PSA-W, Olympus, Japan) with a nominal spring constant of 0,38 N/m were used. Individual spring constants were calibrated for each experiment using the thermal method, and the velocity of the z-piezo was fixed (1 μm /s) for each force *vs.* distance curve. Around 100 force curves were used for determining the local Young´s modulus of each sample, using the Oliver-Pharr model [4.21]:

$$\frac{1-\nu_{\mathrm{sample}}^2}{E_{\mathrm{sample}}} = \frac{1}{E_{\mathrm{eff}}} - \frac{1-\nu_{\mathrm{tip}}^2}{E_{\mathrm{tip}}}$$

assuming that the Poisson ratio of the sample is $\nu_{\mathrm{sample}} = 0.5$ as in previous studies with hydrogel-like samples [4.22-4.24]. Corresponding to a silicon nitride tip, the tip´s Poisson ratio and modulus are $\nu_{\mathrm{tip}} = 0.5$ and $E_{\mathrm{tip}} = 290$ GPa respectively. The physical meaning and calculation of the effective elastic modulus E_{eff} is thoroughly described by the Oliver-Pharr method [4.21]; for calculating E_{eff}, we assumed the correction factors $\beta = 1.05$ [4.25] and $\varepsilon = 0.727$ [4.26]. The indentation area of the tip was calculated for each curve. For this, the tip was defined as a perfect pyramid with an included angle of $\phi = 35°$ given by the cantilever manufacturer. The force curve analysis was conducted using routines from Asylum Research (USA) based on IGOR Pro program, WaveMetrics Inc. (USA). To ensure validity of the measurements, experiments were done at different indentations ranging from 20 nm to 100 nm. In this way, every indentation depth was much smaller than 10% of the sample thickness, and real contact areas were calculated one by one for each indentation.

Note that local Young´s moduli have been calculated applying these AFM nanomechanical tests. The obtained results can not be compared with the Young´s modulus of bone found in the literature [4.27] (ranging from 15 to 25 GPa), because they are typically obtained in bulk by dry measurements. Therefore, the results found in the literature are an overestimation of the real values, as more reliable results are obtained in wet and nanomechanical experiments (as done in the present study). The main reason to measure the Young´s moduli at the nanoscale is that it has been demonstrated that key factors for successful tissue regeneration as cell attachment to the extracellular matrix and cell motility occur at the nanoscale; cells sense, respond and differentiate due to nanoscale topographical and mechanical properties of the matrix [4.28-4.30].

Figure 6 shows histograms corresponding to the values of the local Young´s modulus for chitosan (blue) chitosan/acid-treated SWNTs nanocomposites (black) and chitosan/untreated SWNTs composites (red); all the samples were immersed in a physiological buffer solution as explained before. The mean values are listed in Table 3. Comparing (blue) and (black) it is concluded that incorporation of 80 nm long, acid-treated SWNTs in the chitosan leads to an overall increase of around 100 kPa and a 150 kPa wider distribution in local Young´s moduli values. The effect of 800 nm long, untreated SWNTs in the chitosan matrix is massive, leading to an increase of about 100 times in mean value and a much larger distribution (over 2,500 kPa), probably derived from a more inhomogeneous *zip* structure due to the hydrophobicity of the untreated SWNTs reflected in AFM images. Logically, bundlers of longer SWNTs would be more difficult to deform than smaller, individually wrapped acid-treated SWNTs.

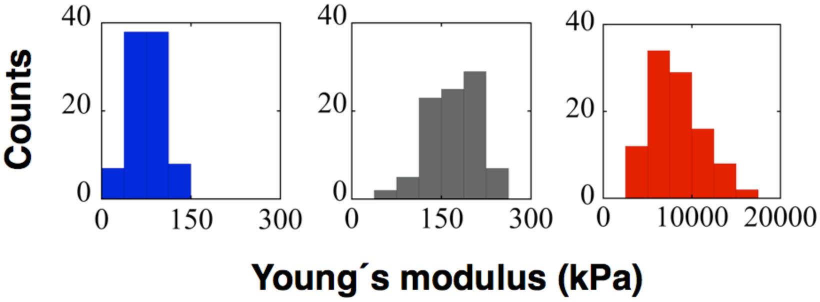

Figure 6 Histograms corresponding to the values of Young´s modulus for chitosan (blue), chitosan containing acid-treated SWNTs (black), and chitosan with untreated SWNTs (red). All the measurements are made in a HEPES buffer at 154 mM NaCl and pH 7.4. Note that the scale of the last histogram is wider than the rest.

Sample	$\langle E \rangle [\mathrm{kPa}]$	$\sigma [\mathrm{kPa}]$
Chitosan	77 ± 3	26 ± 6
C/AT-SWNTs	171 ± 4	42 ± 8
C/U-SWNTs	8198 ± 283	2841 ± 566

Table 3 Mean Young´s modulus (<E>, kPa) and distribution (σ, kPa) obtained by AFM force spectroscopy in chitosan, chitosan containing acid-treated SWNTs (C/AT-SWNTs) and chitosan with untreated SWNTs (C/U-SWNTs).

4.5 Conclusions

It is introduced for the first time the free volume theory to tissue engineering. PALS measurements of scaffolds for tissue engineering provide valuable information regarding nutrient diffusion within these materials, which is a crucial property for cell proliferation in this strategy.

The inclusion of acid-treated SWNTs decreases both the mean free volume hole size and distribution of the chitosan matrix due to the wrapping of the acid-treated SWNTs by the chitosan molecules. The ratio of available free volume holes for oxygen diffusion is increased a 3%, while the ratio of free volume holes available for glucose diffusion is practically null. The analyzed acid-treated SWNTs/chitosan nanocomposites show good pore size for bone tissue engineering applications (≥ 150 μ m). Addition of acid-treated SWNTs to chitosan doubles the mean Young´s modulus of chitosan matrix.

The inclusion of untreated- SWNTs increases both the mean free volume hole size and distribution of the chitosan matrix due to the hydrophobicity and scant defects of raw SWNTs. The ratio of available free volume holes for oxygen diffusion is slightly decreased, while the ratio of free volume holes available for glucose diffusion is doubled. The addition of raw 800 nm sized SWNTs as bundles of longer SWNTs would be more difficult to deform than individually wrapped 80 nm sized acid-treated SWNTs.

CHAPTER 5

THE EFFECT OF CERAMIDE IN THE FREE VOLUME OF DPPC LIPID MEMBRANES

Cell membranes are of great importance in almost all cellular processes and in understanding and treating several diseases. A vast number of different molecules and complexes form membranes in the cell (i.e., outer membrane, nucleus membrane, mitochondria membrane, etc.), but principally lipids and proteins. These lipids are mainly phospholipids forming a lipid bilayer, a polar membrane with a width of few nanometers composed of two lipid layers. Lipid bilayers of cell membranes are key elements in molecular trafficking, and contain ceramides (Cer) at high concentrations. Cer are bioactive waxen lipid molecules crucial in many physiological functions [5.1-5.6]. Some of these processes (as cellular signaling, cell adhesion, differentiation, cell migration or apoptosis - programmed cell death) are linked with Cer-mediated alterations in the biophysical properties of the lipid membrane [5.7-5.9].

It has been also proved that free volume is essential for several structural and dynamic properties of lipid membranes: e.g., packing and ordering of molecules of the bilayer [5.10], diffusion of lipids and proteins in its plane [5.11-5.13] and permeation of small molecules across the membrane [5.14].

Despite the importance of the Cer and the free volume properties in biomembranes, the effect of Cer on free volume holes inside membranes is still unknown. Probably, the experimental adversities in the measurements of subnanometer-sized voids in lipid membranes in a non-perturbative way are the cause of this absence of information. In this line, PALS has been successfully applied since the 80´s decade in measuring the changes in local free volume holes in different biological membranes. Positron annihilation studies have been carried out for studying (i) a phase transition in human red cell ghost membranes [5.15], (ii) the effect of N_2O in dipalmitoylphosphatidylcholine (DPPtdCho) liposomes [5.16], (iii) different structural changes in natural membranes [5.17], (iv) the phase transitions in DPPC [5.18], (v) the phase transitions in DMPC and sphingomyelin [5.19] and (vi) the effect of excess of water in the phase transition of DPPC [5.20]. More recently, in 2009 Sane et al. analyzed the effect of cholesterol in DPPC and POPC lipid membranes by PALS [5.21]. Dong et al. characterized the molecular packing and mobility of the lipid chains by PALS in phytantriol/water bulk phases in 2009 [5.22] and in lamellar phases of DSPC, DPPC, DMPC and DLPC in 2015 [5.23].

The aim of this chapter is to study by PALS how the presence of Cer affects the size and distribution of free volume holes within model lipid membranes, as free volume holes could be linked in the unexplained mechanism of certain Cer properties (i.e., membrane permeabilization, transbilayer lipid movements, also named *flip-flop*, and the release of cytochrome c to the cytosol from mitochondria in apoptosis). Disorders linked to apoptosis are connected to diseases as cancer for which Cer is considered a potential therapeutic target [5.24, 5.25]. Uncovering the biophysical effects of Cer and the processes involved in apoptosis could improve the Cer-related anti-cancer therapies. In addition to PALS, differential scanning calorimetry (DSC) and molecular dynamics computer simulations were also employed to analyze the effect of Cer in DPPC bilayers, the most widely used lipid in model membranes research.

5.1 Materials and sample preparation

5.1.1 Materials

Egg-yolk ceramide (Cer), 1,2-dipalmitoyl-*sn*-glycero-3-phosphocholine (DPPC) and 1,2-dioleoyl-*sn*-glycero-3-phosphocholine (DOPC) from Avanti Polar Lipids (Alabaster, AL, USA) were utilized.

5.1.2 Membrane preparation

The membrane preparation was carried out by Aritz García-Arribas at the Biophysics Unit, UPV/EHU – CSIC by following this specific protocol: multilamellar vesicles (MLVs) were prepared by initially mixing the appropriate amount of synthetic pure lipids dissolved in chloroform/methanol (2:1, v/v). The samples were dried by evaporating the solvent under a stream of nitrogen, then placing them under high vacuum for 2 h. The samples were then hydrated in purified water (lipid:water 40:60 w/w for PALS, 1 mM lipid in buffer for DSC), helping dispersion by stirring with a glass rod and finally extruding the solutions between two syringes through a narrow tubing (0.5 mm internal diameter, 10 cm long) 150 times. The procedure was performed at a temperature well above that of the phase transitions for all compositions.

5.2 Differential Scanning Calorimetry (DSC)

The measurements were performed in a VP-DSC high-sensitivity scanning microcalorimeter (MicroCal, Northampton, MA, USA) in the Biophysics Unit, UPV/EHU – CSIC by Aritz García-Arribas. Both lipid and buffer solutions were fully degassed prior to loading into the appropriate cell in the form of MLVs. MLVs inserted in assay buffer (NaCl 150 mM, 20 mM PIPES, 1 mM EDTA) and at a 1 mM concentration. 0.5 ml at 1 mM total lipid concentration was loaded into the calorimeter, performing three heating scans at a 45 °C/h rate, between 20 and 70 °C for all the samples. Phospholipid concentration was determined as lipid phosphorus, and used together with data from the third scan, to obtain normalized thermograms. The software Origin 7.0 (MicroCal), provided with the calorimeter, was used to determine the different thermodynamic parameters from the scans. The software PeakFit (Systat Software Inc., Chicago, IL, USA) was used for endotherm deconvolution.

Figure 1 shows the DSC thermograms. In this figure, the phase transition from gel phase to fluid phase is determined for DPPC and DPPC:Cer 85:15 mol ratio and Cer. We used DOPC as control, because the gel-fluid transition of DOPC is -17 °C, far below 10 °C, so the sample does not exhibit any endothermic peak at this range. DPPC shows an endothermic peak at around 41 °C, identifying its gel-fluid phase transition. At around 35 °C it is also highlighted a smaller peak, corresponding to the named pre-transition (appearing between the tilted and rippled gel phase). The DPPC:Cer binary mixture exhibits a broad and complicated gel-fluid transition between 30 °C – 55 °C. The endothermic peak is composed by at least three superimposed endothermic peaks, probably associated to the coexisting DPPC:Cer domains of non-uniform composition. For its part, Cer exhibits a tight endothermic peak at around 92 °C, corresponding to its gel to fluid transition. It has been previously reported that normally long-chain Cer increases both the value and the width of single phospholipid gel-fluid transition [5.9,5.26-5.29]. Thus, the present thermogram is in agreement with these studies.

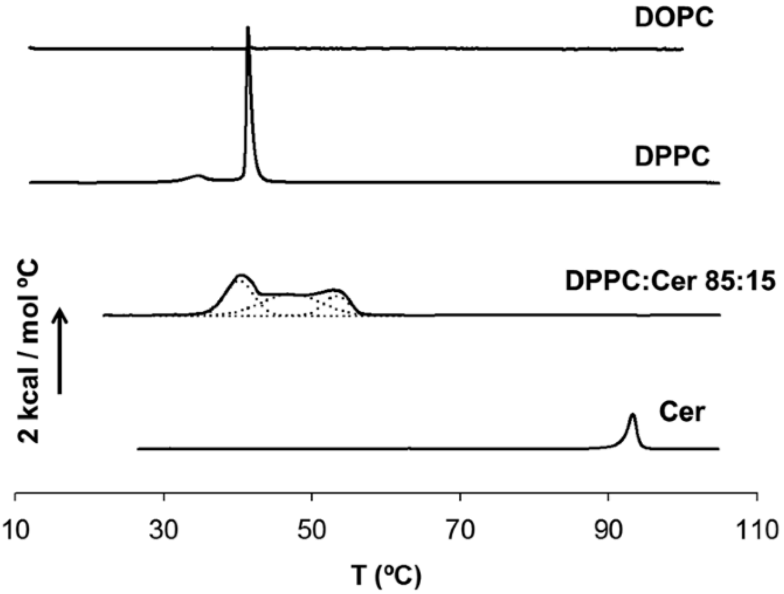

Figure 1 Differential Scanning Calorimetry (DSC) representative thermograms of DOPC, DPPC, DPPC:Cer 85:15 mol ratio and pure Cer aqueous dispersions. Y axis shows heat capacity (Cp) in kcal/mol °C. Dotted lines represent peak fitted endotherms. DPPC Cp values have been divided by a factor of 3 for clarity.

5.3 Positron annihilation lifetime spectroscopy (PALS)

The PALS equipment utilized and the measurement of the free volume void size is described in the first chapter of the present thesis. The source employed was the R1 (please, find more information about this positron source in section 1.1). It is important to note that utilizing our sealed source and biosampler holders described in chapter 1, the sample is not contaminated with the radioactive Na^{22}, at variance with previous PALS works in lipid membranes. The obtained results for ortho-positronium (o-Ps) lifetime and distributions for pure DPPC and DPPC:Cer

85:15 mol ratio at different temperatures are summarized in Table 1.

DPPC		
Temperature (ºC)	$\langle \tau_{o-Ps} \rangle [ns]$	$\sigma [ns]$
15	2.02 ± 0.03	0.35 ± 0.03
25	2.10 ± 0.09	0.34 ± 0.11
30	2.05 ± 0.07	0.47 ± 0.09
37	2.07 ± 0.09	0.60 ± 0.10
39	2.17 ± 0.01	0.61 ± 0.02
41	2.19 ± 0.09	0.63 ± 0.10
43	2.47 ± 0.09	0.73 ± 0.10
45	2.53 ± 0.07	0.71 ± 0.10
50	2.65 ± 0.07	0.69 ± 0.10
60	2.93 ± 0.07	0.46 ± 0.15

DPPC : Cer (85 : 15)		
Temperature (ºC)	$\langle \tau_{o-Ps} \rangle [ns]$	$\sigma [ns]$
20	2.21 ± 0.09	0.42 ± 0.10
30	2.17 ± 0.08	0.76 ± 0.10
34	2.41 ± 0.09	0.47 ± 0.11
38	2.51 ± 0.10	0.60 ± 0.11
44	2.55 ± 0.09	0.61 ± 0.11
55	2.93 ± 0.10	0.63 ± 0.15
60	3.04 ± 0.04	0.73 ± 0.06

Table 1 Mean ortho-Positronium (o-Ps) lifetime and distribution obtained by PALS for DPPC and DPPC:Cer (85:15).

In order to test how does Cer affect the free volume holes of DPPC membranes we employed Tao-Eldrup equation, as previously used in other PALS studies in lipid membranes [5.21-5.24]. Figure 1 shows the results for the mean free volume hole size of pure DPPC and DPPC:Cer 85:15 mol ratio at different temperatures in order to test the differences in the temperature dependence of free volume hole mean size.

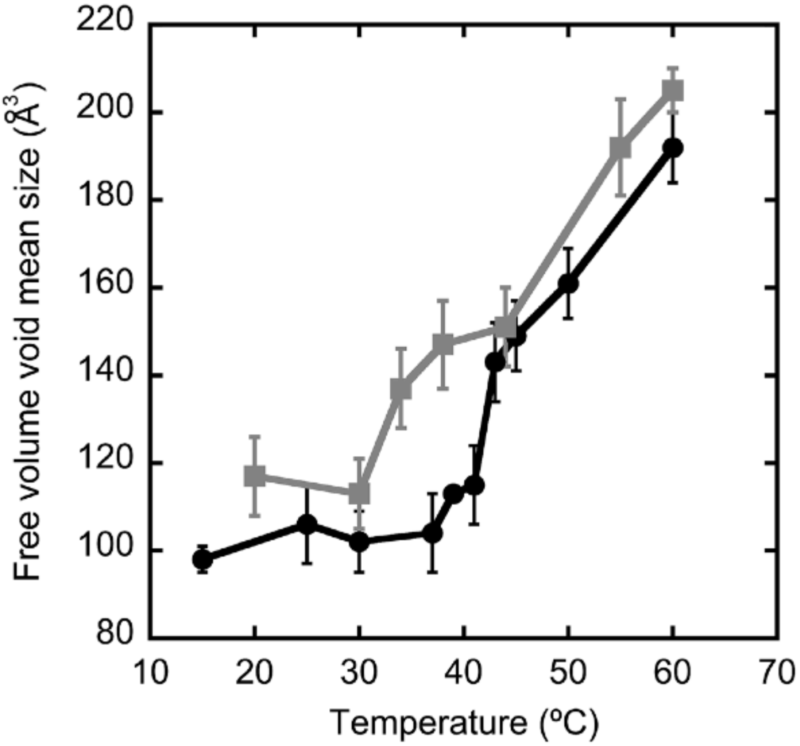

Figure 2 Temperature dependence of free volume void mean size in DPPC membranes (black) and in DPPC:Cer (85:15 mol:mol) (grey).

Figure 2 indicates that in DPPC membranes the mean free volume hole size increases very slightly until 37 °C temperature is reached. At this point, the mean hole size increases abruptly. The greatest slope is highlighted between 41 °C and 43 °C, just at the gel-fluid transition of DPPC recorded in DSC experiments. This result is in agreement with previous studies [5.21]. The

DPPC:Cer binary mixtures show an increased mean free volume hole size at almost all the analyzed temperatures. Between 30 °C and 45 °C the inclusion of Cer provokes the greatest rise in the free volume hole sizes, coinciding in part with the gel-fluid transition temperature of DPPC. At 37 °C, the mean free volume hole size was 104±2 $Å^3$ for DPPC, although for DPPC:Cer the mean free volume hole size at 38 °C was around a 40% larger, 147±2 $Å^3$. Further, the o-Ps lifetime distribution (and consequently the free volume hole size distribution in the membranes) is wider in the presence of Cer.

If we examine in contrast PALS and DSC results from Figure 3, it seems that the abrupt variations in the slope of the mean free volume hole size could be linked to the phase transitions in the lipids; for DPPC there exist clear slope changes in PALS data at the gel-fluid transition, and more subtle slope variations at the pre-transition.

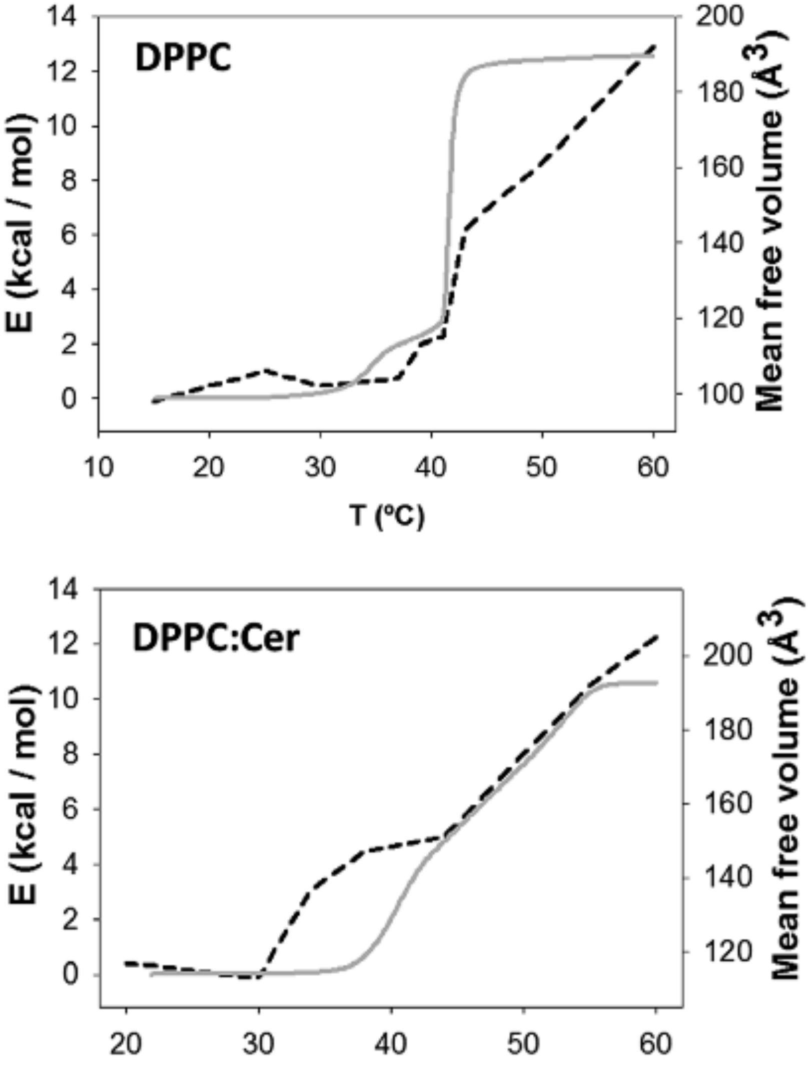

Figure 3 Comparison of integrated thermograms (grey solid line) and PALS mean free volumes (black dashed line) for DPPC (above) and DPPC:Cer 85:15 (below).

Regarding DPPC:Cer binary mixtures, PALS results show that the mean free volume hole size starts to increase abruptly at 30

°C in a complex fashion, coinciding with the starting point of the also complex endothermal transition revealed in DSC experiments (See Figure 1). These results suggest that the presence of Cer-enriched domains could be involved in the commented changes in the free volume hole sizes within DPPC:Cer lipid membranes at 30 °C – 55 °C temperature range. Cer-enriched domains in binary phospholipid:Cer lmembranes containing from 3% to 30% of Cer have been detected by different biophysical methods in several studies [5.29-5.37]. It is noticeable that based on PALS and DSC results we can conclude that from 60 °C on, the phase transition processes are finished.

As demonstrated in very recent studies [5.23], the combination of DSC and PALS techniques gives novel information about the role of the free volume holes within lipid membranes and their phase transitions.

5. 4 Molecular dynamics simulations

In order to gain more information about the effect of Cer in the free volume holes of DPPC membranes, molecular dynamics simulations were carried out by Jon Iñaki Mujika in the Faculty of Chemistry of the UPV/EHU and the Donostia International Physics Center (DIPC). DPPC and DPPC+C16:0 model membranes in solution were investigated at four temperatures: 20 °C, 30 °C, 37 °C and 52 °C. The initial structure and topology files for the DPPC in solution were obtained from the website of the Biocomputing group of the University of Calgary (Canada) [5.38]. The model membranes are composed of 128 DPPC lipids, 64 per leaflet. For the DPPC+Cer binary mixtures, 24 DPPC molecules were replaced by Cer molecules, obtaining mixtures containing a 18% Cer in DPPC. The force field parameters for Cer were fixed from a topology file downloaded from Roland Faller's Research Group´s (University of California - Davis, USA) website [5.39]. The lipids were *solvated* by adding a total of 5726 SPC model water molecules. The version 4.5.3 [5.40,5.41] of the Gromacs package was used to run the molecular dynamics simulations. All the computational technical details of the simulations are described elsewhere [5.42]. A total run of 100 ns simulation time was employed for the production stage of each simulation. Logically, the number of molecules is not enough to represent macro, or even microscale phase separation due to the present limitations in computational capacity.

In order to characterize the free volume, a grid-based method was used based on a previous work [5.21]. A rectangular box grid is defined in 3D for a certain structure, and the number of free grids counted. A grid is not considered to be free when at least one atom is within its van der Waals radius. The grid element length was defined to be 1.6 Å, since the diameter of the positronium is 1.59 Å. The average sizes of the holes were calculated from the molecular dynamics simulations in order to compare them with those obtained from PALS experiments. Even from the same simulation, free volume hole sizes differed for different snapshots caused by the fluctuations and dynamics within the membranes. Taking into account this fact, 10 different snapshots were extracted from the last 10 ns of each simulation (one every 1ns), and the average void size and standard deviation was determined for each simulation.

Figure 4 shows the lipid molecules utilized in the atomistic molecular dynamics (MD) simulations of DPPC and DPPC:Cer binary mixtures in solution. The final structures at 20 ºC, 30 ºC, 37 ºC and 52 ºC are shown in Figure 5.

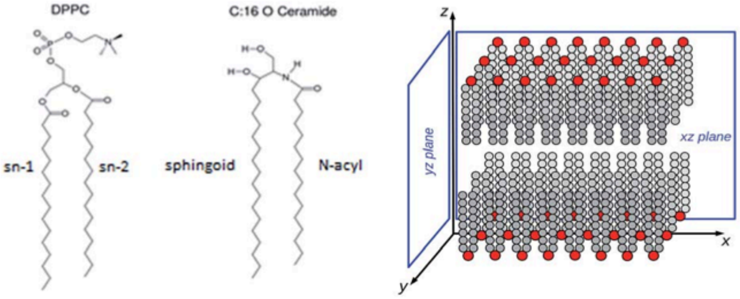

Figure 4 Left, schematic representation of the two lipid molecules included in the atomistic molecular dynamics simulations. Right, definition of the Z axis mentioned in the main text and in Figure 6.

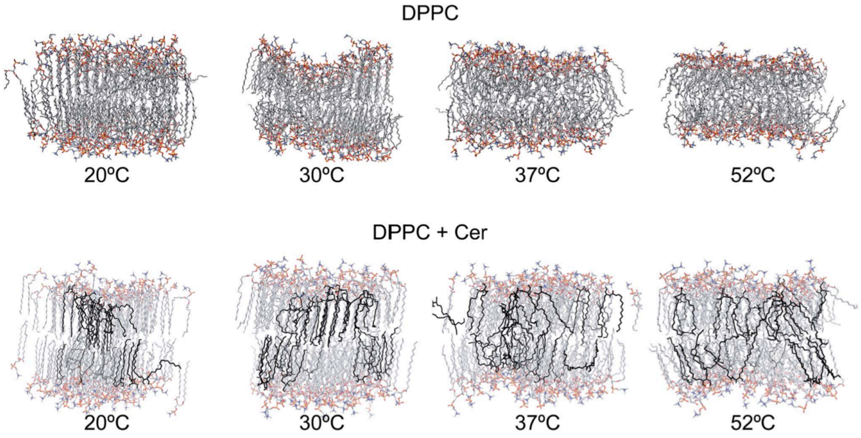

Figure 5 Final snapshots corresponding to the 100 ns atomistic molecular dynamics simulations carried out for DPPC in water (above) and DPPC + Cer in water (below) at four temperatures: 20 ºC, 30 ºC, 37 ºC and 52 ºC. Cer molecules are shown in black. Note that water molecules are not represented.

Figure 6 shows the electron density of DPPC and DPPC:Cer at different temperatures. Even being shorter the Cer molecule in comparison with DPPC, when Cer is present the electron density in the inter layer area (when Z axis is around 0 Å) clearly decreases. At the same time, the bilayers thickness is larger with Cer (see also Figure 5), which tipically means a higher ordering. In this line, it can be observed that for both DPPC and DPPC:Cer, the larger the temperature, the thinner the bilayer. Regarding the location of the Cer, the electron density profiles for Cer (Figure 6, orange solid lines) suggest that the Cer molecules are mostly located in zones where the tails of DPPC molecules predominate, probably caused by their high hydrophobicity. This is in accordance with several studies that define Cer as a molecule that increases molecular order along the lipid tails [5.30-5.33,5.43]. With all this, from MD simulations it is concluded that Cer increases the ordering of the DPPC, which is in agreement with previous studies about the inclusion of Cer in other lipids as POPC or DMPC [5.44,5.45]. Regarding the pre-transition of DPPC, snapshots of DPPC bilayers at 37 °C show a fluid-like state; this is in agreement with PALS results as the mean free volume hole sizes start to grow at 35 °C, until an intense increase at 41 °C, the main gel-fluid transition. Finally, in relation with the Cer domains, the snapshots for DPPC:Cer shows regions in which Cer is abundant (even if are not pure Cer domains), particularly at 20 °C and 30 °C.

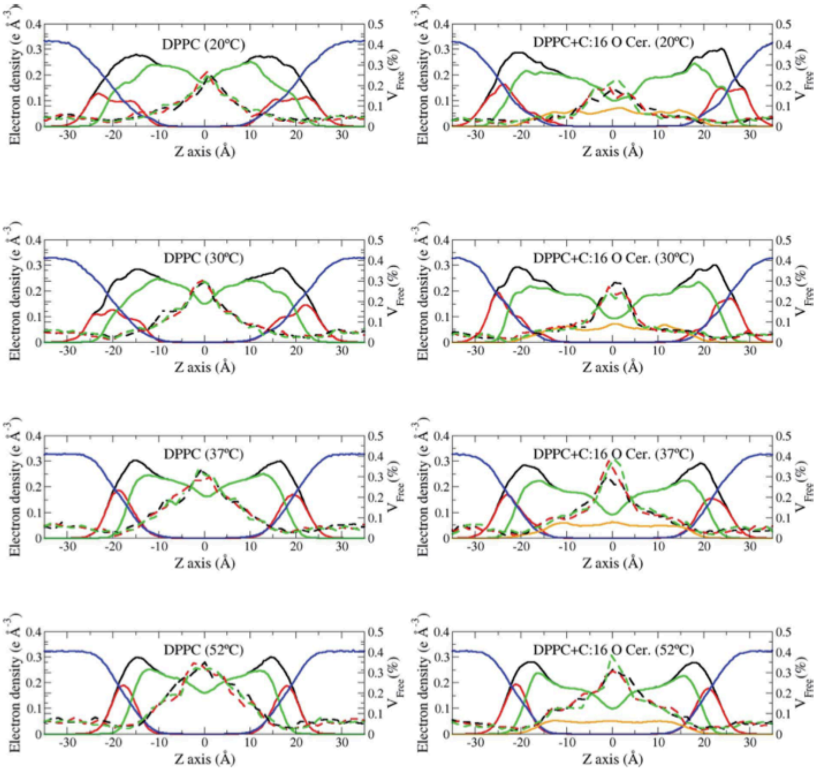

Figure 6 Electron density profiles (in e/Å^3) along the Z axis calculated for the last 10 ns of the molecular dynamics

simulations of DPPC (left) and DPPC + Cer (right) systems at four temperatures (in descending order): 20 °C, 30 °C, 37 °C and 52 °C. DPPC (solid black), DPPC heads (solid red), DPPC tails (solid green), water (solid blue) and Cer (solid orange). The relative free cell distribution with respect to the Z axis length computed in the last three snapshots extracted from the simulations are shown in dashed lines.

The relative distributions of free volume holes (free cells) with respect to the Z axis are also plotted by dashed lines in Figure 6. In DPPC alone, as supposed, the free volume is majorly placed in the space between the two layers, while is almost null when the number of DPPC headgroups is high. At 20 °C and 30 °C the line reflects a narrow peak, so the free volume is concentrated at the layer interface. Nonetheless, at 37 °C and 52 °C a wider peak appears; then, at these temperatures the free volume holes are more distributed in the zone of the lipid tails. In DPPC:Cer binary mixtures, the free volume hole distribution changes. At 20 °C and 30 °C, the free volume holes are mainly placed between the layers too. But as the distance between the lipid tails is larger, the peak is wider: so the inclusion of Cer enhances the number of free spaces that free cells can occupy. At 37 °C and 52 °C, even though the free volume distribution increases in this region, the peak is narrower: so, again, the free volume is located mainly between the layers.

5.5 Comparison of MD simulations and PALS results

In order to directly compare MD simulations and PALS results, Figure 7 plots the average free volume hole size computed for each sample. It is important to note that the obtained values of the average hole size are significantly smaller comparing to the values obtained by PALS probably as a result of the total size difference between the experimental samples and the MD simulations models. However, the trends are similar and the results are in accordance in a qualitative way: (i) the mean free volume hole size values increase with the temperature. (ii) In both cases, Cer enlarges the mean free volume void size, especially at 37 °C. (iii) At 52 °C, the values for DPPC and DPPC:Cer are very similar in both MD simulations and PALS.

Finally, the three largest holes for the final snapshot of the simulations at 37 °C are plotted in Figure 8. In DPPC:Cer binary mixtures the holes are undoubtedly larger than for DPPC alone. The enlargement of the holes in the presence of Cer is occurring mostly due to the larger free volume located at the plane between the two layers.

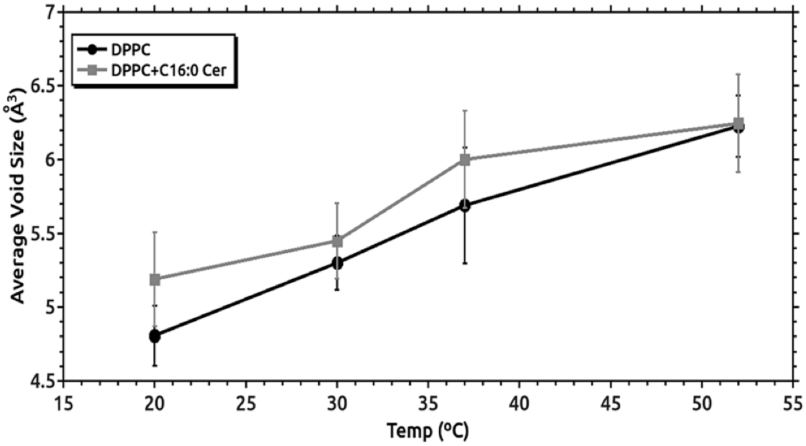

Figure 7 Computational calculation of average void size (in Å3) at 20 °C, 30 °C, 37 °C and 52 °C for the DPPC (in black) and DPPC + Cer (in grey) systems.

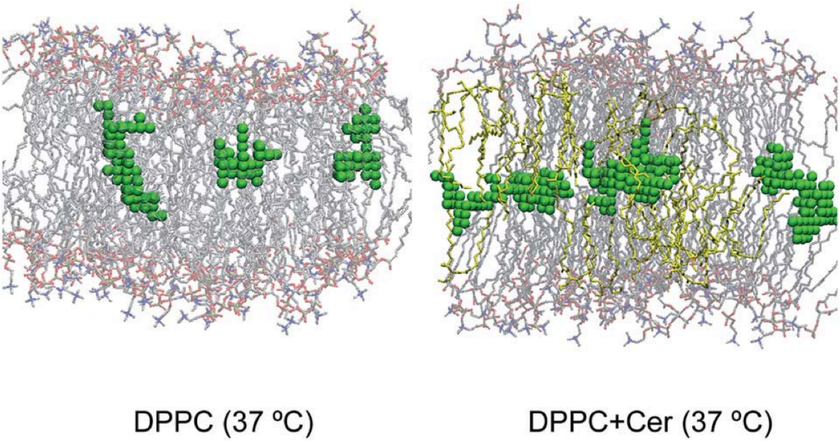

Figure 8 Representation of the final snapshots from the 100 ns atomistic molecular dynamics simulation for the DPPC (on the left) and DPPC + Cer (on the right) systems at 37 ºC. Cer molecules are shown in yellow. The three largest voids determined in each system are shown in green.

Even though it is well known that Cer increases the permeability of lipid bilayers and increases the solute flow, the underlying mechanisms are unknown. The present chapter of this thesis would elucidate this, as an increment in the free volume hole size could imply and increment in the molecular diffusion and maybe of the permeability. Another theory is the formation of Cer channels [5.46,5.47], but PALS results did not detect the presence of bigger pores.

MD results highlight an increase in the size of the free volume holes, even without the formation of Cer-rich domains. This fact is interesting, as it permits to suggest that the effect of Cer in the free volume holes could not be focused in the Cer-rich domains, but in the surrounding continuous phase. Traditionally, the biophysical effects have been attributed to the Cer domains as they present high packing and nanomechanical strength. But in this case it seems that the imperfect packing between the Cer domains and the surrounding phase could increase the free volume hole sizes.

5.6 Conclusions

The effect of Cer on DPPC lipid bilayers can be summarized as an ordering effect that increases the size and distribution of the free volume holes. Adding 15 mol% Cer to DPPC, the mean free volume void size increases up to 40% at the physiological temperature.

By following the free volume theory, this fact implies that the presence of Cer significantly increases the molecular diffusion within the DPPC membranes. Then, we could speculate that this increment in the free volume hole size of biomembranes is influencing unexplained Cer-promoted, biological membrane related processes (i.e., lipid *flip-flop* motion, the increase in the membrane permeability or the release of cytochrome c to the cytosol from mitochondria in apoptosis).

Results highlight that the combination of PALS, DSC and molecular dynamics simulations is a powerful strategy for characterizing and understanding the role of free volume in biological membranes.

CHAPTER 6

FIRST PALS STUDY FOR THE CHARACTERIZATION OF LIVING CELLS

In the last few decades, several positron annihilation studies in biotechnology, bioengineering and biomolecular systems have been done [6.1]. As an example, in the previous chapters accomplishments of PALS applications in polymers with potential medical uses, scaffolds for tissue engineering and biological membranes have been described. In this line, PALS has been recently applied to cancer research, too. Cancer is a major health related problem in our society: nowadays, cancer is causing 1 in 8 deaths worldwide [6.2]. Deaths from cancer are projected to continue rising and estimated to be more than 13 million deaths in 2030 [6.3]. Molecular biology has successfully led several strategies to fight cancer; however, there are a lot of cancers without an adequate treatment. Physics is a fresh discipline in the field, and is constantly providing new insights about the nature of cancer, which hopefully will help fighting cancer in the future [6.4]. Physics and mechanics of cancer cells are undoubtedly connected to their biology. A better understanding of the physical properties of cancer cells is explaining, for example, their movement within the extracellular matrix, or their division. In this line, PALS is currently applied to cancer samples in order to gain information about the physics of cancer. Here are summarized all the investigations (still scarce) regarding positron annihilation spectroscopy applications to cancer research:

(i) In 2006, significant differences between human healthy skin samples and cancerous skin cancer samples (basal and squamous cell carcinomas) in the o-Ps lifetimes and intensities were reported in an outstanding work of the group leaded by Y. C. Jean. These measurements were carried with dried samples under high vacuum. They proposed PALS as a potential medical tool for the detection of skin cancer at early stages in an external and non-invasive way [6.5].

(ii) In 2007, the same group published again differences between the human healthy skin samples and skin cancer samples (basal and squamous cell carcinomas) in the probability density functions (see Chapter 4 of the present thesis). In this case, experiments were made under ambient conditions with water moisture in order to make the measurement in a more physiological environment [6.6].

(iii) In 2008, this group from the University of Missouri-Kansas City (USA) reported slight differences in the o-Ps lifetime (but more clear in the intensity) between healthy skin and melanoma samples, and proposed an in-vivo experiment with animal models in order to gain information about the selectivity of positron annihilation to cancer formation [6.7].

(iv) In 2009, C. A. Quarles and his group from the Texas Christian University (USA), applied PALS to rat healthy brain and rat glioma samples soaked in formalin. No significant differences were detected in the o-Ps lifetimes, probably due to the use of formalin [6.8].

(v) In the same year, a group from the Institute for Theoretical and Experimental Physics of Moscow (Russia) leaded by S. V. Stepanov proposed a strategy for the detection of carcinogens based on the Positronium formation [6.9,6.10].

Currently, the existing methods in detecting cancer are mainly imaging devices via an internal approach (such as PET, capable to detect millimeter size tumors) and via invasive biopsy techniques. Therefore, in the author of this thesis opinion, the proposal of applying PALS as an early skin cancer detection method by an external and non-invasive way is especially remarkable. However, biological tissues (as skin) are complex and very heterogeneous materials, which limits the use of PALS to these types of samples. Indeed, cellular composition of tissue samples varies from the same organism and may involve changes in the PALS results, even if the tissue samples are coming from the same animal or patient. Further, even in a single tumor, in addition to different biological matter (vessels, adipose tissue, etc), there exists an extreme heterogeneity of cell populations. As the sensitivity of PALS is excellent as perceives very small changes in the free volume holes, and due to the heterogeneity of biopsy samples, extracted PALS data can be confusing and non-reproducible.

The elastic modulus measured by AFM has been demonstrated to be a fingerprint of cancer [6.11], it would be also very interesting to test if the free volume measured by PALS would also be a molecular fingerprint of cancer. As described in the present thesis, free volume holes play a key role in a variety of mechanical properties in polymers, and dynamic processes in biological systems. The role of the free volume holes within the cells (cytoplasm, nucleus, etc) is completely unknown, and PALS seems to be a good technique to characterize it, as it has successfully provide a direct measurement of the dynamic free volume hole sizes and distributions in different biological systems. Due to the unbeatable sensitivity of PALS, the author of this thesis with the inestimable help of Ainara Castellanos-Rubio hypothesized that PALS would be more useful in detecting more specific changes in the same cell line rather than in detecting differences between healthy/cancerous biopsies. For example, would it be possible to detect by PALS biological responses to environmental factors, such as cellular differentiation and changes in cell colony structure?

To test this idea, we applied PALS to an unique cell line, T84 human colon cancer cells, under two different environmental conditions that result in distinct *in vitro* multicellular organization of colonies. Cells were grown within a type I collagen gel matrix (3D cell culture model) with or without transforming growth factor β (TGF-β). TGF-β is a fibroblast-derived factor affecting epithelial cell proliferation, differentiation, motility, and T84 cell differentiation. Cells in collagen form unorganized 3D cell clusters within the gels, but when grown in the presence of TGF-β, T84 epithelial cells are able to organize and differentiate into a distinct phenotype that resembles intestinal crypts [6.12]. In this way, we could analyze the specific response in terms of the mean free volume hole size and distribution of the living cells under two different, specific environmental conditions.

6.1 3D Cell cultures

The cell cultures were carried out by Ainara Castellanos-Rubio and Tamara Lopez-Euba in the Hospital of Cruces in Barakaldo, by the following protocol:

Human colon adenocarcinoma T84 cell line (CCL 248, ATCC Rockville, MD, USA) was kindly provided by Prof. Markku Maki (Celiac Disease Study Group, University of Tampere, Finland). Cells were maintained in culture in the laboratory. Dulbecco's modified Eagle's medium F12 nutrient mixture (1:1) (DMEM-F12 ref 31330), penicillin-streptomycin (ref 15070) and sodium bicarbonate were purchased from Life Technologies (Spain). Heat inactivated foetal bovine serum (ref F9665), 10× RPMI-1640 (ref R1145), trypsin/EDTA (ref T4049), Triton X-100 (ref T9284), albumim from bovine serum (ref B4287) and ribonuclease A (ref R6513) were obtained from Sigma-Aldrich (Spain). Rat tail Collagen I (ref 354236) was purchased from Beckton Dickinson (Spain). Transforming growth factor beta 1 recombinant human (rhTGF-β, ref 240-B) was purchased from R&D systems (United Kingdom) and paraformaldehyde (ref 15710) from electron microscopy sciences, Hoetch 33342 and phalloidin-PE were obtained from Sigma-Aldrich (Spain). Plastic dishes were obtained from Corning Costar (Spain) and plates from Becton Dickinson (Spain).

Cells were maintained in culture medium composed of DMEM-F12, 5% heat inactivated foetal bovine serum and 1% penicillin-streptomycin [6.12]. T84 cells were grown on T75 tissue culture flasks at 37°C in a 5% CO_2 atmosphere and passaged once a week upon reaching 80% confluence. Culture medium was changed every 2 days. T84 cells were removed from the flasks with 6 ml 0,25% trypsin-EDTA at 37°C during 15 minutes. Then, were washed in medium, collected by centrifugation at 450G during 5 minutes and subcultured in 24-well plates with collagen. Cells in suspension were counted with a cellular counter (*Coulter particle count and size analyser*, Beckman Coulter). T84 cells were plated in 24 well plates at a density of 1.5×10^5 cells/well.

For generating 3D aggregates rat tail Collagen I was used. Collagen was mixed with acetic acid, 10× RPMI-1640 and sodium bicarbonate. In each experiment we used 1 ml collagen, 125 µl RPMI-1640 10× and 125 µl sodium bicarbonate.

To create the 3D culture, 300 µl of the collagen mix (3 mg/ml final concentration) were added to each well and incubated at 37°C to jellify. After 20 minutes of incubation, cells were resuspended in additional 200 µl of the collagen mix and were seeded on collagen gels. Finally, 1 ml DMEM-F12 culture medium was added to cover 3D cultures.

To determine the optimal length of the experiments (i.e. the suitable time in the cell cultures to measure their mean free volume through PALS) we have chosen different culture times to make measurements: 6-13-20-27-34-41 days.

To induce changes in cell morphology, T84 aggregates were incubated with 10 ng/ml hrTGF-β1 added to the culture medium [6.12]. These cultures were grown in culture until 41 days and the culture medium was changed every two days.

6.2 Immunofluorescence microscopy

The experiments were performed by the author of this thesis and Tamara Lopez-Euba with the helpful assistance of the SGIKER staff of the UPV/EHU. 7 and 17 day-old 3D cell cultures were fixed with 4% paraformaldehyde at room temperature for 30 minutes. After washing three times with phosphate-buffered saline (PBS), cultures were permeabilized with 0.5% Triton X-100 at 4°C overnight and washed again with PBS. Following blocking with 3% bovine serum albumin (BSA) in PBS at room temperature during 2 hours, cultures were incubated with RnaseA 1× (1:1000) at room temperature for 1 hour [6.13]. Filamentous actin was labeled with phalloidin-PE (1:1000) at 4°C overnight [6.14]. Cell nuclei were stained with Hoechst 33342 (1:1000) at 4°C for 3 hours.

Samples were analyzed with an Olympus Fluoview FV500 confocal microscope. Stack deconvolution and 3D reconstruction of images taken on the z axis to construct motion videos were performed with ImageJ software.

As expected, T84 intestinal epithelial cells grown in 3D form unorganized round colonies in 7 and 17 day-old cultures (see Figure 1, control). Cells are unpolarized and accumulated around in clusters without any organized orientation. Cell nuclei are distributed around the colony, but in an unorganized manner (for more graphic information, watch the confocal microscopy videos S1 and S2 published elsewhere). Nevertheless, when T84 cells are grown in 3D in the presence of TGF -β, cell colonies present a highly organized structure, as a one-cell layer around a central lumen (see Figure 1, TGF-β. For more graphic information, watch the confocal microscopy videos S3 and S4 published elsewhere [6.15]). Filamentous actin distribution (Figure 1, C) are localized in the lining of the spherical lumens, reflecting TGF-β mediated differentiation (for more information, see the videos S3 and S4).

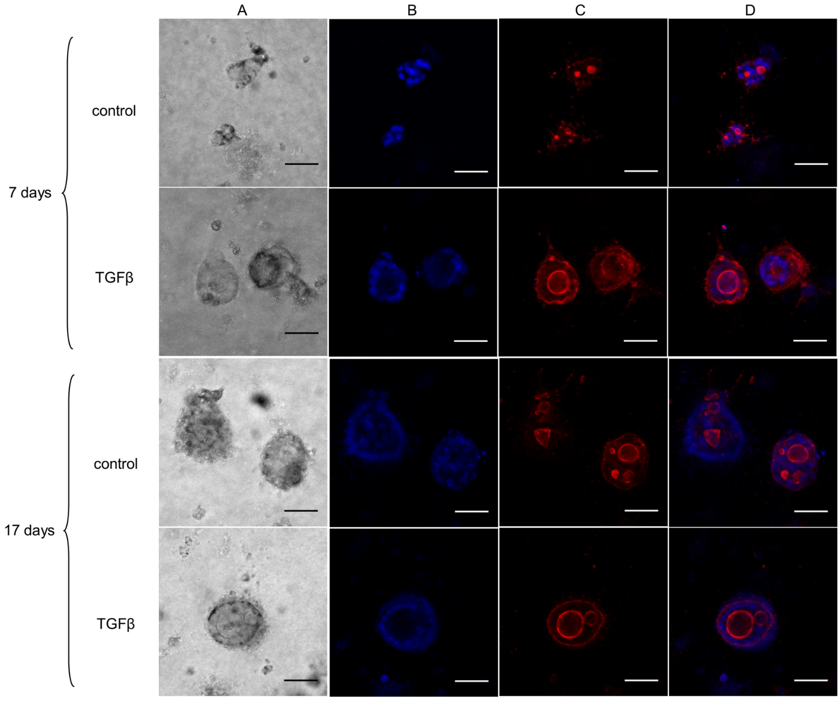

Figure 1 Effect of TGF-β on T84 3D epithelial cell organization. Confocal microscopy of 7 and 17 day-old T84 in three-dimensional culture. All images are at 20× magnification. Scale bar represent 50 μm. (A) T84 colonies are observed with phase contrast. (B) Cell nuclei stained with Hoechst. (C) Filamentous actin is stained with phalloidin-PE. In (D), merged images of B and C.

6. 3 Free volume hole size measurements

The PALS equipment utilized and the measurement of the free volume void size is described in the first chapter of the present thesis. The source employed was the R1 one (for more information about this source, check section 1.1). The designed and fabricated biosample holder allowed us to measure fresh, living cell cultures. The measurements were conducted at 4°C. The lifetime of positrons remained unchanged along the time by the exposition to the source radiation during three measurements, confirming the reproducibility of the experiment.

PALS results are summed up in Table 1. The mean lifetime and distribution of *o*-Ps in 3D cell cultures were respectively 2–12% and 20–120% larger than in collagen (Table 1); this means that positron signal is coming from cells in the 3D cultures. Depending on the growth time point, the *o*-Ps lifetime distribution for TGF-β cultures was between 0.11±0.08 ns to 0.26±0.07 ns larger than under unstimulated growth conditions. We used the Tao-Eldrup model for polymers when calculating the sizes of free volume voids from the *o*-Ps lifetime, as previously done in many PALS studies in biological systems [6.5-6.8,6.16,6.17] and in terms of free volume hole sizes, in both unstimulated and TGF-β growth conditions the holes volumes of the 3D cultures increased to reach a maximum (Figure 2); for normal growth conditions the mean hole volume in the peak was 102±1 Å^3 at 34 days, while for the culture with TGF-β was 111±1 Å^3 at 20 days. As shown in Figure 2, once the mean hole size reached a maximun, this value started to decrease gradually: the mean hole volume decreased 7% under normal conditions in 1 week, and 16% in 3 weeks under TGF-β conditions.

	Collagen		Control		TGF-B	
Growth time (days)	$\langle \tau_{o-Ps} \rangle [ns]$	$\sigma [ns]$	$\langle \tau_{o-Ps} \rangle [ns]$	$\sigma [ns]$	$\langle \tau_{o-Ps} \rangle [ns]$	$\sigma [ns]$
**	1.92 ± 0.02	0.20 ± 0.04	-	-	-	-
6	-	-	1.95 ± 0.03	0.28 ± 0.05	1.99 ± 0.02	0.39 ± 0.03
13	-	-	1.96 ± 0.01	0.29 ± 0.02	2.03 ± 0.03	0.55 ± 0.05
20	-	-	1.99 ± 0.03	0.24 ± 0.06	2.15 ± 0.01	0.47 ± 0.01
27	-	-	-	-	2.03 ± 0.02	0.42 ± 0.03
34	-	-	2.06 ± 0.01	0.37 ± 0.01	1.97 ± 0.03	0.48 ± 0.04
41	-	-	1.98 ± 0.02	0.30 ± 0.04	1.97 ± 0.03	0.44 ± 0.04

Table 1 *o*-Ps mean lifetime ($\langle \tau_{o-Ps} \rangle$) and distribution ($\sigma$, ns) in collagen I and T84 human colonic adenocarcinoma three-dimensional cell cultures grown in normal conditions and with TGF-β, at different growth time points.

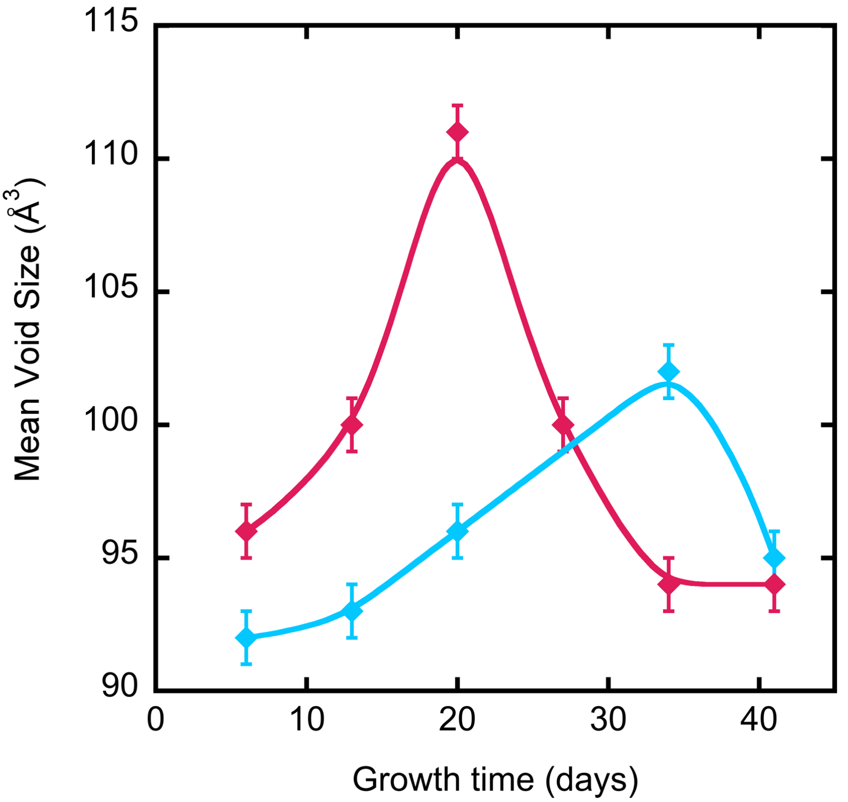

Figure 2 Growth time dependence of mean void volume in human colonic adenocarcinoma T84 3D cell cultures. The blue curve represents control cultures and the red curve represents cultures treated with TGF-β.

It is found that PALS detects atomic scale changes of the mean free-volume void size in human colonic adenocarcinoma 3D cell cultures over time. PALS measurements suggest that morphological changes observed by immunofluorescence microscopy in cell cultures in different conditions are the consequence of molecular events that are taking place in the cells. Although cell culture developmental events can not be correlated directly to the free volume, results imply that cellular changes are indeed reflected in the nanostructure of these cultures. The *o*-Ps lifetime changes probably emerge from the dynamic processes of cell cultures (growth, division and death). Furthermore, TGF-β induces cell differentiation, and this is accompanied by an increase in the distribution of *o*-Ps lifetime (and thus, of free volume size) in the 3D cell cultures. This result implies a greater dispersion of hole size in samples treated with TGF-β compared to unstimulated conditions. Cell death could be involved in the drop in the *o*-Ps lifetimes.

We are at the dawn of PALS applications in complex cell systems, but our results show that 3D cell cultures (*o*-Ps lifetime is measured in a mixture of cells and collagen, there is not any complex tissue as in biopsies) can be a good starting point for this type of research. To the best of author´s knowledge, this is the first study of the application of PALS in 3D living cell cultures. Indeed, this study opens the doors to more measurements in different cell lines and culture conditions that modify different and specific biological parameters. Currently, PALS only allows bulk measurements that do not provide sufficient resolution to distinguish *o*-Ps lifetimes in individual cells from the whole culture, and much less in different parts of the cell. Nonetheless, in this particular case, the measured increase in lifetimes and distributions must be due to molecular and structural changes that affect the free volume of the cells and consequently that of the 3D culture. Furthermore, PALS is a non-perturbative technique; it perturbs neither the structure of the 3D culture nor cell dynamics. Together with the experimental research, studies to show whether the local electric fields caused by transmembrane voltage of the cells are affecting the positron signal, or which parts of the cell are preferred targets for the positron annihilation should be also undertaken. Additionally, computational simulations to evaluate the fit of the Tao-Eldrup model (implemented for free-volume characterization in polymers) into different parts of the cell will be necessary, cytosol (the fluid enclosed within the cell membrane) would be an interesting starting point.

6.4 Conclusions

This is the first study applying PALS for the characterization of living cells. Our results demonstrate that the 3D cell cultures are useful for measuring free volume in living cells by PALS in a realistic and controlled way, and for the observation of changes in free volume void sizes in cell cultures due to specific factors (e.g., growth time and TGF-β).

This study is in agreement with PALS technique as a valid tool for the characterization of biological systems and could provide useful information in cancer research at the atomic and molecular scale.

FINAL CONCLUSIONS

A positron annihilation lifetime spectrometer as well as a sample holder for measuring biological samples in the range 4 °C – 80 °C have been designed and fabricated for the Nuclear Techniques Laboratory of the UPV/EHU. By using this equipment, the free volume hole size and distribution of different biomaterials and biological matter have been successful measured in order to understand the role of free volume in these systems. It is concluded that:

1 The enlargement of the size of the free volume holes caused by gamma irradiation improves the shape memory recovery process of polycyclooctene shape memory polymers with potential biomedical applications.

2 The concept of the molecular transport via free volume diffusion in tissue engineering materials has been introduced for the first time. Changes in the free volume properties of chitosan scaffolds have been detected by PALS when inserting carbon nanotubes.

3 The presence of Ceramide in model DPPC membranes increases the mean free volume hole size within the lipid bilayers.

4 The pioneering application of PALS in living cells has been successfully carried out. Biological changes alter the free volume properties of T84 colon adenocarcinoma cells in 3D cultures.

LIST OF PUBLICATIONS

Some parts of the work made in the development of the present thesis have derived to the publication of 4 papers in journals that are in the top 25% of their ISI categories:

[1] *Sub-nanoscale free volume and local elastic modulus of chitosan nanocomposite scaffolds for tissue engineering*
Eneko Axpe, Loic Bugnicourt, Maite Goiriena-Goikoetxea, Iraultza Unzueta, David Merida, Jose Angel Garcia, Fernando Plazaola and Sonia Contera, *Journal of Materials Chemistry B,* 3 (16), 3169-3176 (2015).

[2] *Ceramide increases free volume voids in DPPC membranes*
Eneko Axpe, Aritz B García-Arribas, Jon Iñaki Mujika, David Mérida, Alicia Alonso, Xabier Lopez, Jose Angel Garcia, Jesus M Ugalde, Felix M Goñi and Fernando Plazaola, *RSC Advances*, 5 (55), 44282-44290 (2015).

[3] *Connecting free volume with shape memory properties in noncytotoxic, gamma-irradiated polycyclooctene*
Eneko Axpe, Nuria García-Huete, José María Cuevas, Clarisse Ribeiro, David Mérida, José Manuel Laza, Senentxu Lanceros-Méndez, José Ángel García, José Luis Vilas, Luis Manuel León and Fernando Plazaola, *Journal of Polymers Science Part B: Polymers Physics*, 53 (15), 1080-1088 (2015).

[4] *Detection of atomic scale changes in the free volume void size of 3D colorectal cancer cell culture using positron annihilation lifetime spectroscopy*
Eneko Axpe, Tamara Lopez-Euba, Ainara Castellanos-Rubio, David Merida, Jose Angel Garcia, Leticia Plaza-Izurieta, Nora Fernandez-Jimenez, Fernando Plazaola and Jose Ramon Bilbao, *PLoS ONE*, 9, 1 (2014).

REFERENCES

CHAPTER 1

[1.1] Y. P. Yampolskii, *Russ Chem Rev*, 2007, **76**, 59-78.

[1.2] Y. C. Jean, P. E. Mallon and D. M. Schrader, *Principles and applications of positron and positronium chemistry*, 2003, Wold Scientific.

[1.3] D. M. Schrader and Y. C. Jean, *Positron and positronium chemistry*, 1998, Elsevier.

[1.4] Mina Roussenova, Doctoral Thesis, *Molecular organization and mobility in glass forming systems – a free volume perspective*, University of Bristol, 2011

[1.5] M. Charlton and J.W. Humberston, *Positron Physics*, 2001, Cambridge University Press.

[1.6] K. Saarinen, P. Hautojarvi and C. Corbel, *Positron Annihilation Spectroscopy of Defects in Semiconductors*, 2001, Academic Press.

[1.7] P. A. M. Dirac, *P Roy Soc Lond A Mat*, 1928, **117**, 610-624.

[1.8] C. D. Anderson, *Phys Rev*, 1993, **43**, 491-494.

[1.9] O. E. Mogensen, *J Chem Phys*, 1974, **60**, 998-1004.

[1.10] O. E. Mogensen, *Positron Annihilation in Chemistry*, 1995, Springer-Verlag.

[1.11] M. Deutsch, *Phys Rev*, 1951, **82**, 455-456.

[1.12] T. Goworek, *J Nucl Radiochem Sci*, 2000, **1**, 11-13.

[1.13] J Kansy, *Nucl Instrum Meth A*, 1996, **374**, 235-244.

[1.14] R. M. Nieminen and M. J. Manninen, *Positron in solids*, 1979, Springer-Verlag.

[1.15] S. J. Tao, *J Chem Phys*, 1972, **56**, 5499-5510.

[1.16] M. Eldrup and D. Ligthbody and N. J. Sherwood, *J Chem Phys*, 1981, **63**, 51-58.

[1.17] B. Jasinska, A. E. Koziol and T. Goworek, *Acta Phys Pol A*, 1999, **95**, 557-561.

[1.18] D. W. Gidley, W. E. Frieze, T. L. Dull, A. F. Yee, E. T. Ryan and H. M. Ho, *Phys Rev B*, 1999, **60**, R5157-R5160.

[1.19] H. Nakanishi, S. J. Wang and Y. C. Jean, *Positron annihilation studies of fluids*, 1988, World Scientific.

[1.20] Dupasquier A., *Positronium like systems in solids*, *in Positron Spectroscopy of Solids*, Dupasquier A., and Mills A.P., Jr. Eds., IOS Press, Amsterdam, 1985, 510-564.

[1.21] Gidley D.W., Peng H.G., Vallery R.S., 2006, *Annu Rev Mater Res*, **36**, 49-79.

[1.22] F. Plazaola, E. Axpe, D. Merida, J.A. Garcia, *Técnicas de aniquilación de positrones en el estudio de materiales poliméricos, in Caracterización de materiales aislantes poliméricos para uso eléctrico*, O.A. Lambri Editor, UNR Editora, Argentina, 2012, 31-67.

CHAPTER 2

[2.1] Diogenes Laërtius, probably 3rd century AD, *Democritus*, **9**, 44.

[2.2] D. Sedley, *Phronesis*, 1982, **27**, 175-193.

[2.3] A. J. Z. Batschinski, *Physik Chem*, 1913, **84**, 643-706.

[2.4] H. J. Eyring, *J Chem Phys*, 1931, **4**, 283-291.

[2.5] H. J. Eyring and O. Hirschfelder, *J Chem Phys*, 1937, **41**, 249-257.

[2.6] J. E. Lennard-Jones and A. F. Devonshire, *Proc R Soc Lond A*, 1938, **165**, 1-11.

[2.7] J. H. Irving and J. G. Kirkwood, *J Chem Phys*, 1950, **18**, 817-829.

[2.8] Z. W. Salsburg and J. G. Kirkwood, *J Chem Phys*, 1952, **20**, 1538-1543.

[2.9] T. G. Fox and P. J. Flory, *J Appl Phys*, 1950, **21**, 581-591.

[2.10] J. Doolittle, *J Appl Phys*, 1951, **22**, 1471-1475.

[2.11] M. H. Cohen and D. Turnbull, *J Chem Phys*, 1959, **31**, 1164-1169.

[2.12] M. Roussenova, Doctoral Thesis, *Molecular organization and mobility in glass forming systems – a free volume perspective*, University of Bristol, 2011.

[2.13] J. Frenkel, Kinetic theory of liquids, Oxford University Press, London, 1946.

[2.14] G. Dlubek, D. Kilburn, V. Bondarenko, J. Pionteck, R. Krause-Rehberg and M. A. Alam, Nichkristalline Strukturen DGK Jena, 2003. Published in Internet: http://www.uni-jena.de/chemie/DGK-AK4/

[2.15] A. Bondi, *J Phys Chem*, 1964, **68**, 441-451.

[2.16] D. Van Krevlen, *Properties of polymers*, Elsevier, 1976.

[2.17] R. Simha R and G. Carri, J Polym Sci Part B: Polym Phys, 1994, **32**, 2645-2651.

[2.18] A. Bondi, *Physical properties of molecular crystals, liquids and glasses*, Wiley, 1968.

[2.19] S. Putta and S. Nemat-Nasser, *Mater Sci Eng A*, 2001,

317, 70-76.

[2.20] H. J. Limbach and J. Ubbink, Soft Matter, 2008, 4, 1887-1898.

[2.21] F. Beuche, *J Chem Phys*, 1953, **21**, 1850-1855.

[2.22] V. B. Gupta, C. Brahatheeswaran, *Polymer*, 1991, **32**, 1875-1884.

[2.23] C. A. Kusmins and T. K. Kwei, *Diffusion in polymers*, Academic London, 1968.

[2.24] J. S. Vrentas and J. L. Duda, *J Polym Sci*, 1977, **15**, 403-416.

[2.25] M. H. Cohen and G. S. Grest, *Phys Rev B*, 1979, **20**, 1077-1098.

CHAPTER 3

[3.1] H. J. Qi, T. D. Nguyen, F. Castro, C. M. Yakacki and R. Shandas, *J Mech Phys Solids*, 2008, **56**, 1730-1751.

[3.2] A. Lendlein, H. Jiang, O. Jünger and Robert Langer, *Nature*, 2005, **434**, 879-882.

[3.3] Y. Liu, H. Lv, X. Lan, J. Leng and S. Du, *Compos Sci Technol*, 2009, **69**, 2064-2068.

[3.4] W. M. Huang and B. Yang, *Appl Phys Lett*, 2005, **98**, 114105-1-3.

[3.5] X. J. Han, Z. Q. Dong, M. M. Fan, Y. Liu, J. H. Li, Y. F. Wang, Q. J. Yuan, B. J. Li and S. Zhang, *Macromol Rapid Comm*, 2012, **33**, 1055-1060.

[3.6] P. R. Buckley, G. H. McKinley, T. S. Wilson, W. Small, W. J. Benett, J. P. Bearinger, M. W. McElfresh and D. J. Maitland, *IEEE Trans Biomed Eng*, 2006, **53**, 2075-2083.

[3.7] Y. Liu, H. Du, L. Liu and J. Leng, *Smart Mater Struct*, 2014, **23**, 023001-1-22.

[3.8] J. Hu, H. Meng, G. Li and S. I. Ibekwe, *Smart Mater Struct*, 2012, **21**, 053001-1-23.

[3.9] A. Charlesby, *Atomic Radiation and Polymers*, Pergamon Press, 1960, 198-257.

[3.10] M. Anthamatten, S. Roddecha and J. Li, *Macromol*, 2013, **46**, 4230-4234.

[3.11] S. Hayashi, Y. Tasaka, N. Hayashi and Y. Akita, *Mitsubishi Heavy Industries*, Ltd. Technical Review, 2004, **41**, 1-3.

[3.12] W. Sokolowski, A. Metcalfe, S. Hayashi, L. Yahia and J. Raymond, *Biomed Mater*, 2007, **2**, S23-S27.

[3.13] Compound Summary for CID 6641, *Pub Chem*, Open Chemistry Database.

[3.14] H. J. Radusch, I. Kolesov, U. Gohs and G. Heinrich, *Macromol Mater Eng*, 2012, **297**, 1225-1234.

[3.15] N. Garcia-Huete, J. M. Laza, J. M. Cuevas, J. L. Vilas, E. Bilbao and L. M. Leon, *Radiat Phys Che*, 2014, **102**, 108-116.

[3.16] S. M. Tamboli, S. T. Mhaske and D. D. Kale, *Indian J Chem Technol*, 2004, **11**, 853-864.

[3.17] A. Oshima, S. Ikeda, T. Seguchi and Y. Tabata, *Radiat Phys Chem*, 1997, **49**, 279-284.

[3.18] A. Lendlein and S. Kelch, *Angew Chen Int Edit*, 2002, **41**, 2034-2057.

[3.19] K. Ito, K. Abe, H. L. Li, Y. Ujihira, N. Ishikawa, S. Hayashi, *J Radioanal Nucl Chem*, 1996, **211**, 53–60.

[3.20] J. Fuchs, Environmental stressors in health and disease, CRC Press, 2001.

[3.21] A. Lendlein, Shape-memory polymers, Springer Science & Business Media, 2010.

[3.22] A. Garle, S. Kong, U. Ojha, B. M. Budhlall, *ACS Appl Mater Interfaces*, 2012, **4**, 645–657.

[3.23] G. Barot and I. J. Rao, *Zeitschrift für Angew Math und Phys*, ZAMP, 2006, **57**, 652-681.

CHAPTER 4

[4.1] A. Khademhosseini, J. P. Vacanti and R. Langer, *Sci Am*, 2009, **30**, 64-71.

[4.2] R. Langer and J. P. Vacanti, *Science*, 1993, **260**, 920-926.

[4.3] J. O´Brien, *Mater Today*, 2011, **14**, 88-95.

[4.4] U. Del Monte, *Cell Cycle*, 2009, **8**, 505-506.

[4.5] E. W. Thiele, *Industrial and Engineering Chemistry*, 1939, **31**, 916-920.

[4.6] H. L. Lv, B. G. Wang and Y. Kong, *Polym J*, 2009, **41**, 1049-1054.

[4.7] F. Croisier and C. Jerome, *Eur Polym J*, 2013, **49**, 780-792.

[4.8] M. Dash, F. Chiellini, R. M. Ottenbrite and E. Chiellini, *Prog Polym Sci*, 2011, **36**, 981-1014.

[4.9] A. R. Costa-Pinto, R. L. Reis and N. M. Neves, *Tissue Eng Part B-Re*, 2011, **17**, 331-347.

[4.10] W. W. Thein-Han and R. D. K. Misra, *Mater Sci Tech Ser*, 2008, **34**, 1062-1075.

[4.11] W. W. Thein-Han, J. Saikhun, C. Pholpramoo, R. D. K. Misra and Y. Kitiyanant, *Acta Biomater*, 2009, **9**, 3453-3466.

[4.12] L. Carson, C. Kelly-Brown, M. Stewart, A. Oki, G. Regisford, Z. P. Luo and V. I. Bakhmutov, *Mater Lett*, 2009, **63**, 617-620.

[4.13] I. Olivas-Armendariz, P. Garcia-Casillas, R. Martinez-Sanchez, A. Martinez-Villafane and C. A. Martinez-Perez, *J Alloy Compd*, 2010, **495**, 592-595.

[4.14] C. M. Agrawal, J. L. Ong, M. R. Appleford and G. Mani, *Cambridge Texts in Biomedical Engineering*, 2013.

[4.15] Y. L. Liu, W. H. Chen and Y. H. Chang, *Carbohyd Polym*, 2009, **76**, 232-238.

[4.16] J. Venkatesan, Z. J. Qian, B. Ryu, N. A. Kumar and S. K. Kim, *Carbohyd Polym*, 2011, **83**, 569-577.

[4.17] W. Xiao, T. Wu, J. Peng, Y. Bai, J. Li, G. Lai, Y. Wu and L. Dai, *J Appl Polym Sci*, 2013, **128**, 1193-1199.

[4.18] D. Turnbull and M. H. Cohen, *J Chem Phys*, 1961, **34**, 120-125.

[4.19] A. Bondi, Physical Properties of Molecular Crystals, *Liquids and Glasses*, Wiley, New York, 1968.

[4.20] P. Neogi, *Diffusion in polymers,* Marcel Dekker, New York, 1996.

[4.21] W. C. Oliver and G. M. Pharr, *J Mater Res*, 1992, **7**, 1564-1583.

[4.22] K. Urayama, T. Takigawa and T. Masuda, *Macromolecules*, 1993, **26**, 3092-3096.

[4.23] B. D. Johnson, D. J. Beebe and W. Crone, *Mat Sci Eng C-Bio S*, 2004, **24**, 575-581.

[4.24] S. P. Marra, K. T. Ramesh and A. S. Douglas, *Mat Sci Eng C-Bio S*, 2001, **14**, 25-34.

[4.25] W. C. Oliver and G. M. Pharr, *J Mater Res*, 2004, **19**, 3-20.

[4.26] Y. H. Hu, J. O. You, D. T. Auguste, Z. G. Suo and J. J. Vlassak, *J Mater Res*, 2012, **27**, 152-160.

[4.27] R. O. Ritchie, M. J. Buehler and P. Hansma, *Phys Today*, 2009, **62**, 41-47.

[4.28] N. Huebsch, P. R. Arany, A. S. Mao, D. Shvartsman, O. A. Ali, S. A. Bencherif, J. Rivera-Feliciano and D. J. Mooney, *Nat Mater,* 2010, **9,** 518-526.

[4.29] P. Kanchanawong, G. Shtengel, A. M. Pasapera, E. B. Ramko, M. W. Davidson, H. F. Hess and C. M. Waterman, *Nature,* 2010, **468,** 580-584.

[4.30] G. Maheshwari, G. Brown, D. A. Lauffenburger, A. Wells and L. G.Griffith, *J Cell Sci,* 2000, **113,** 1677-1686.

CHAPTER 5

[5.1] A. Gómez-Muñoz, *Biochim Biophys Acta*, 1998, **1391**, 92–109.

[5.2] Y. A. Hannun, C. R. Loomis, A. H. Merrill Jr and R. M. Bell, *J Biol Chem*, 1986, **261**, 12604–12609.

[5.3] A. Merrill, A. Sereni, V. Stevens, Y. Hannun, R. Bell and J. Kinkade, *J Biol Chem*, 1986, **261**, 12610–12615.

[5.4] R. N. Kolesnick, *J Biol Chem*, 1987, **262**, 16759–16762.

[5.5] S. N. Pinto, L. C. Silva, A. H. Futerman and M. Prieto, *Biochim Biophys Acta*, 2011, **1808**, 2753–2760.

[5.6] L. M. Obeid, C. M. Linardic, L. A. Karolak and Y. A. Hannun, *Science*, 1993, **259**, 1769–1771.

[5.7] A. Cremesti, F. Paris, H. Grassme, N. Holler, J. Tschopp, Z. Fuks, E. Gulbins and R. Kolesnick, *J Biol Chem*, 2001, **276**, 23954–23961.

[5.8] R. Kolesnick, *J Clin Invest*, 2002, **110**, 3–8.

[5.9] F. M. Goñi and A. Alonso, *Biochim Biophys Acta Biomembr*, 2009, **1788**, 169–177.

[5.10] M. Kupiainen, E. Falck, S. Ollila, P. Niemelä, A. Gurtovenko, M. Hyvönen, M. Patra, M. Karttunen and I. Vattulainen, *J Comput Theor Nanosci*, 2005, **2**, 401–413.

[5.11] M. Javanainen, L. Monticelli, J. B. de la Serna and I. Vattulainen, *Langmuir*, 2010, **26**, 15436–15444.

[5.12] S. J. Marrink and H. J. Berendsen, *J Phys Chem*, 1996, **100**, 16729–16738.

[5.13] P. Almeida and W. Vaz, *Handb Biol Phys*, 1995, **1**, 305–357.

[5.14] D. Bemporad, C. Luttmann and J. Essex, *Biophys J*, 2004, **87**, 1–13.

[5.15] E. I. H. Chow, S. Y. Chuang and P. K. Tseng, *Biochim Biophys Acta Biomembr,* 1981, **646**, 356-359.

[5.16] H. Costabal, *Contrib Cient Technol*, 1984, **15**, 19-24.

[5.17] J. C. Glass, G. Graf, H. Costabal, D. H. Ewert and L. English, *Positrons in biomolecular systems. II Membranes*, 1982, 930-931.

[5.18] Y. C. Jean and A. J. Hancock, *J Chem Phys*, 1982, **77**, 5836-5839.

[5.19] S. Sung, T. Mahmood, Y. C. Jean, M. F. Lou and D. Borchman, *Positron and Positronium Chemistry Int Workshop*, 1990, 454-459.

[5.20] S. Baluch, J. Cirak and P. Balgavy, *Stud Biophys*, 1990, **136**, 65-70.

[5.21] P. Sane, E. Salonen, E. Falck, J. Repakova, F. Tuomisto, J. M. Holopainen and I. Vattulainen, *J Phys Chem B*, 2009, **113**, 1810–1812.

[5.22] A. W. Dong, C. Pascual-Izarra, S. J. Pas, A. J. Hill, B. J. Boyd and C. J. Drummond, *J Phys Chem B*, 2009, **113**, 84-91.

[5.23] A. W. Dong, C. Fong, L. J. Waddington, A. J. Hill, B. J. Boyd and C. J. Drummond, *Phys Chem Chem Phys*, 2015, **17**, 276-286.

[5.24] P. Sane, F. Tuomisto, S. K. Wiedmer, T. Nyman, I. Vattulainen and J. M. Holopainen, *BBA – Biomembranes*, 2010, **5**, 958-965.

[5.25] S. A. Morad and M. C. Cabot, *Nat Rev Cancer*, 2012, **13**, 51–65.

[5.26] J. Sot, F. J. Aranda, M. Collado, F. M. Goñi and A. Alonso, *Biophys J*, 2005, **88**, 3368–3380.

[5.27] J. Sot, L. A. Bagatolli, F. M. Goni and A. Alonso*, Biophys J*, 2006, **90**, 903–914.

[5.28] N. Jiménez-Rojo, A. B. García-Arribas, J. Sot, A. Alonso and F. M. Goñi, *Biochim Biophys Acta*, Biomembr, 2014, **1838**, 456–464.

[5.29] D. C. Carrer and B. Maggio, *J Lipid Res*, 1999, **40**, 1978–1989.

[5.30] J. M. Holopainen, M. Subramanian and P. K. Kinnunen, *Biochemistry*, 1998, **37**, 17562–17570.

[5.31] L. C. Silva, R. F. de Almeida, B. M. Castro, A. Fedorov and M. Prieto, *Biophys J*, 2007, **92**, 502–516.

[5.32] S. S. Leung, J. V. Busto, A. Keyvanloo, F. M. Goni and J. Thewalt, *Biophysical journal,* 2012, **103**, 2465–2474.

[5.33] Y. W. Hsueh, R. Giles, N. Kitson and J. Thewalt, *Biophys J*, 2002, **82**, 3089–3095.

[5.34] H. W. Huang, E. M. Goldberg and R. Zidovetzki, *Biochem Biophys Res Commun*, 1996, **220**, 834–838.

[5.35] J. V. Busto, M. L. Fanani, L. De Tullio, J. Sot, B. Maggio, F. M. Goñi and A. Alonso, *Biophys J*, 2009, **97**, 2717–2726.

[5.36] M. Fidorra, L. Duelund, C. Leidy, A. C. Simonsen and L. A. Bagatolli, *Biophys J*, 2006, **90**, 4437–4451.

[5.37] M. P. Veiga, J. L. R. Arrondo, F. M. Goñi and A. Alonso, *Biophys J*, 1999, **76**, 342–350.

[5.38] Peter Tieleman's Biocomputing Group, http://www.ucalgary.ca/tieleman/?page=Structures_and_Topologies (accessed June 2014).

[5.39] Roland Faller Research Group, http://www.chms.ucdavis.edu/research/web/faller/(accessed June 2014).

[5.40] D. Van Der Spoel, E. Lindahl, B. Hess, G. Groenhof, A. E. Mark and H. J. Berendsen, *J Comput Chem*, 2005, **26**, 1701–1718.

[5.41] B. Hess, C. Kutzner, D. Van Der Spoel and E. Lindahl, *J Chem Theory Comput*, 2008, **4**, 435–447.

[5.42] E. Axpe, A. B. García-Arribas, J. I. Mujika, D. Mérida, A. Alonso, X. Lopez, J. A. García, J. M. Ugalde, F. M. Goñi and F. Plazaola, *RSC Adv*, 2015, **5**, 44282-44290.

[5.43] D. C. Carrer and B. Maggio, *J Lipid Res*, 1999, **40**, 1978–1989.

[5.44] B. Dutagaci, J. Becker-Baldus, J. D. Faraldo-Gomez and C. Glaubitz, *Biochimica et biophysica acta*, 2014, **1838**, 2511–2519.

[5.45] S. A. Pandit, S.-W. Chiu, E. Jakobsson, A. Grama and H. Scott, *Biophys J*, 2007, **92**, 920–927.

[5.46] L. J. Siskind, R. N. Kolesnick and M. Colombini, *J Biol Chem*, 2002, **277**, 26796–26803.

[5.47] L. J. Siskind, R. N. Kolesnick and M. Colombini, *Mitochondrion*, 2006, **6**, 118–125.

CHAPTER 6

[6.1] H. Chen, J. D. Van Horn and Y. C. Jean, *Defect and diffusion forum*, 2012, **331**, 275-293.

[6.2] *Information and resources of cancer*, American Cancer Society, 2012.

[6.3] *Globocan 2008*, IARC, World Health Organization, 2010.

[6.4] D. Wirtz, K.Konstantopoulos and P. C. Searson, *Nat Rev Can*, 2011, **11**, 512-522.

[6.5] Y.C. Jean, Y. Li, G. Liu, H. Chen, J. Zhang and J. E. Gadzia, *Appl Surf Sci*, 2006, **252**, 3166-3171.

[6.6] G. Liu, H. Chen, L. Chakka, J. E. Gadzia and Y. C. Jean, *Phys Stat Sol*, **4**, 3912-3915.

[6.7] G. Liu, H. Chen, L. Chakka, M. L. Cheng, J. E. Gadzia, R. Suzuki, T. Ohdaira, N. Oshima and Y. C. Jean, *Appl Surf Sci*, 2008, **255**, 115-118.

[6.8] S. H. Yang, C. Ballman and C. A. Quarles, *AIP Conf Proc*, 2009, **1099**, 948-951.

[6.9] V. M. Byakov, S. V. Stepanov and O. P. Stepanova, *Mat Sci Forum*, 2009, **607**, 223-226.

[6.10] V. M. Byakov, S. V. Stepanov, O. P. Stepanova, *Phys Status Solidi C*, 2009, **6**, 2503-2506.

[6.11] M Lekka, *Nat Nanotechnol*, 2012, **7**, 691-692.

[6.12] T. Halttunen, A. Marttinen, I. Rantala, H. Kainulainen and M. Mäki, *Gastroenterol*, 1996, **111**, 1252-1262.

[6.13] L. E. O´Brien, W. Yu, K. Tang, T. S. Jou, M. M. P. Zegers and K. E. Mostov, *Methods Enzymol*, 2006, **406**, 676-691.

[6.14] K. Juuti-Uusitalo, L. J. Klunder, K. A. Sjollema, K. Mackovicova, R. Ohgaki, D. Hoekstra, J. Dekker and S. C. D. van IJzendoorn, *PLOS ONE*, 2011, **6**, e22967.

[6.15] E. Axpe, T. Lopez-Euba, A. Castellanos-Rubio, D. Merida, J. A. Garcia, L. Plaza-Izurieta, N. Fernandez-Jimenez, F. Plazaola and J. R. Bilbao, *Plos ONE*, 2014, **9**, e83838.

[6.16] S. Siles, G. Moya, X. H. Li, J. Kansy and P. Moser, *J Radioanal Nucl Chem*, 1999, **240**, 529-530.

[6.17] P. Sane, F. Tuomisto, S. K. Wiedmer, T. Nyman, I. Vattulainen and J. M. Holopainen, *Biochim Biophys Acta*, **1798**, 958-965.